Seton Hall University

eRepository @ Seton Hall

Spring 5-20-2021

Experimental Investigation of Surface Resistivity of Yttrium Stabilized Zirconium as a Thin Film

Matthew J. Melfi
melfimat@shu.edu

Follow this and additional works at: https://scholarship.shu.edu/dissertations

Part of the Ceramic Materials Commons, Nanoscience and Nanotechnology Commons, and the Semiconductor and Optical Materials Commons

Experimental Investigation of Surface Resistivity of Yttrium Stabilized Zirconium as a Thin

Film

By

Matthew J. Melfi

Submitted in partial fulfillment of the requirements for the degree

Master of Science

Department of Physics

Seton Hall University

May 2021

Seton Hall University

Collage of Arts and Sciences

Department of Physics

Approval for Successful Defense

Matthew J. Melfi has successfully defended and made the required modifications to the text of the master's thesis for the M.S. during this Spring semester 2021.

Master's Committee

(Please sign and date beside your name)

Mentor:

Dr. M. Alper Sahiner _____

Committee Member:

Dr. Erie Morales _____

Committee Member:

Dr. Stephen Kelty _____

The mentor and any other committee members who wish to review revisions will sign and data this document only when revisions have been completed. Please return this form to the Office of Graduate Studies, where I will be placed in the candidate's file and submit a copy with your final thesis to be bound as page number two.

Acknowledgement

I would like to thank Seton Hall University for being my place of educational home since the Fall 2016 semester, giving me the opportunity to obtain a Bachelor of Science in Physics and now a Master of Science in Physics as well. I would like to thank all the professors that I have had over my time in Seton Hall. They each have helped and grown me in a particular manner. I would like specially to thank Dr. Sahiner, Dr. Morales, and Dr. Kelty for being part of my thesis committee. I would also like to thank my family for the constant encouragement throughout the years and pushing me to accomplish this goal. I also would like to thank the Advanced Material Synthesis and Characterization Lab (AMSCL) for their help over the years.

Table of Content

Contents

List of Tables

List of Figures

List of Equations

Abstract

Solid Oxide Fuel Cells are devices that use electrochemical reactions to convert chemical energy from fuel to electricity. In comparison with coal power plants, a Solid Oxide Fuel Cell, produces a higher electrical conversion efficiency. However, at higher temperatures (1000°C) it creates a lower ionic conductivity, which limit the Solid Oxide Fuel Cells. When lowering the temperature, the ohmic resistance increases. In our research, an Yttrium Stabilized Zirconium layer will be produced from a fine dimple grain structure allowing high flow of oxygen mobility. This mobility increases ionic conductivity and decrease ohmic loss. The goal of our research is first to determine the surface resistivity for the simulated Yttrium Stabilized Zirconium structures optimize the experimental film deposition parameters that will lead to minimum surface resistivity in these films Yttrium Stabilized Zirconium thin film synthesis using pulsed laser deposition leads to minimize ohmic resistance of the films at optimum film thickness. We will use Zirconium, Al_2O_3, and Silicon substrates for the Yttrium Stabilized Zirconium films and compare the properties of the Yttrium Stabilized Zirconium layer. The thin films will be characterized through electrical measurements such as 4-point probe resistivity measurements as well as Scanning Electron Microscopy, for the structural characterization.

Fuel Cell

Fuel Cells is a drastically new approach in making electrical power that can be powered by a vast number of fuels. But this new production of electricity is like no other. A fuel cell consists of three different layers, the anode, electrolyte, and cathode layers. From the cathode, Oxygen, in either the pure form or from air, is reduced to the oxygen ions [1]. The fuel for these Fuel Cells can be a range of fuels. For instance, the fuel can be any ordinary fuel, but H_2 (*Hydrogen*) is the typical fuel used and the oxidant in the reaction is O (*Oxygen*), from air. In a typical configuration, the fuel is piped through the anode, negatively charged, and the oxidant is piped through the cathode, positively charged. For instance, if H_2 enters the anode the chemical reaction and separates into the positive ions and electrons. From this reaction produces an extreme amount of heat. Then the ions travel through the electrode and then unites with the oxidant in the cathode. The product from this reaction is water. This process can be simplified by looking at the following equations [2].
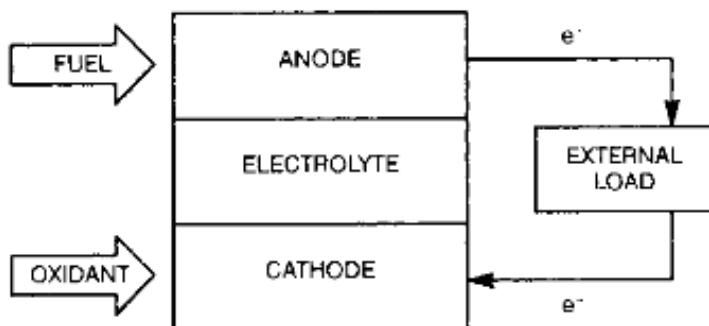
[3] Adapted from Ceramic Fuel Cells

Figure 1: Schematic of a fuel cell.
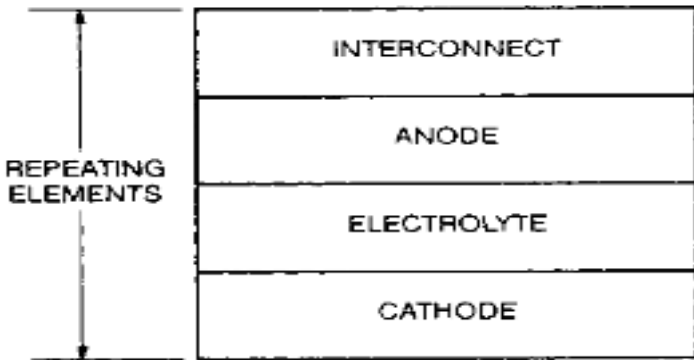
[3] Adapted from Ceramic Fuel Cells

Figure 2: Fuel cell components.

Anode: $H_2 \rightarrow 2H^+ + 2e^-$
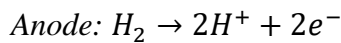
Equation 1: Equation for the Anode

Cathode: $2H^+ + \frac{1}{2}O_2 + 2e^- \rightarrow H_2O$
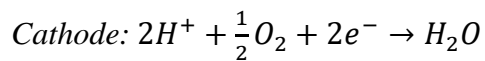
Equation 2: Equation for the Cathode

Total: $H_2 + \frac{1}{2}O_2 \rightarrow H_2O$
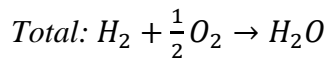
Equation 3: Equation for the Anode and Cathode

The current production of electricity from Fuel Cells is DC (Direct Current). Most applications that use DC need a DC-DC converter. This DC-DC converter converts the output from the Fuel Cell into required voltage and currents for the system. If AC (Alternate Current) is needed an inverter is used to convert the electricity. However, a single Fuel Cell produces not enough energy for many applications. But Fuel Cells can be joined, like batteries, to produce higher power [4].

Production of Hydrogen from Methanol

As shown from earlier, fuel cells need hydrogen or hydrogen rich duel to produce electricity. The only exhaust from this process is water vapor and carbon dioxide. One way of producing hydrogen is to extract the hydrogen from hydrogen rich compounds. In mobile applications, methanol, CH_3OH or CH_4O, has been identified as a suitable fuel source. Current

methanol reformers are usually fixed-bed catalytic reactors. However, with this process has hot and cold spots that are in the catalyst which restricts performance. This process uses both an endothermic and exothermic reaction. The endothermic methanol steam reforming with the exothermic combustion of methanol or hydrogen containing gas from the fuel cell ensuring good heat transfer characteristics which are beneficial for the dynamical response at start-up and during transient.
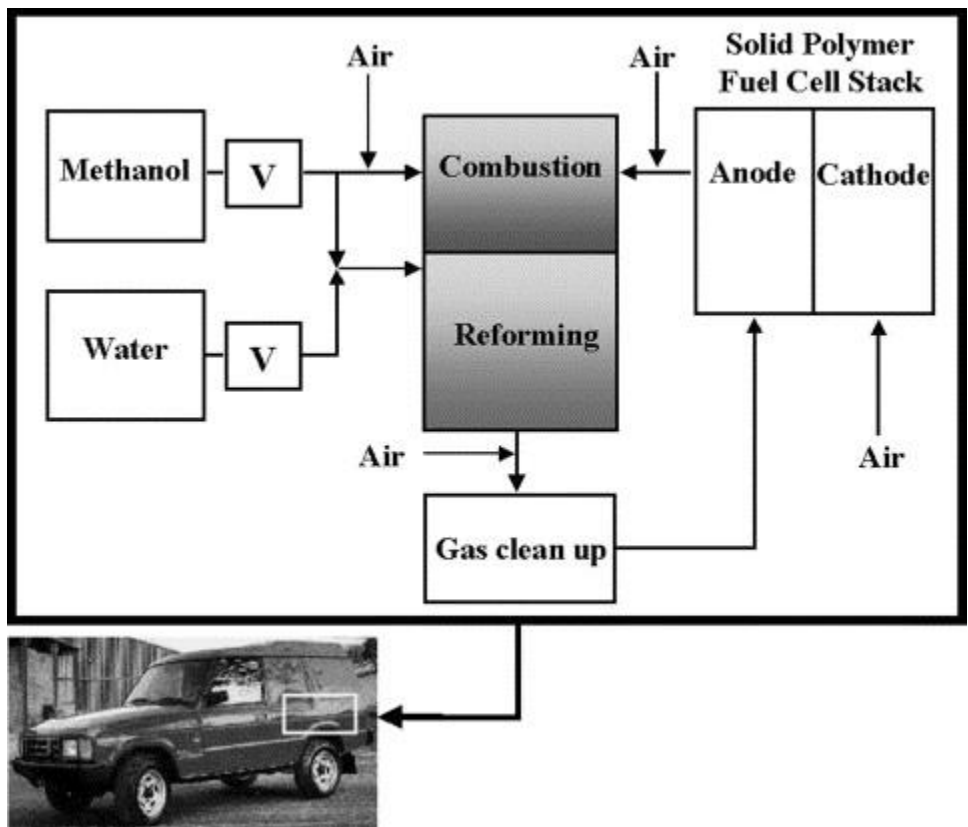
[5]

Adapted from Catalytic production of hydrogen from methanol

Figure 3: Reforming process of methanol and water

This process is feed and consists of vaporized methanol and water. Part of the methanol vapor and hydrogen from the fuel cell anode off gas is mixed with air and catalytically combusted in the combustion section of the system to generate the heat for the steam reforming of methanol

in the reforming section. The hot flue gas from the combustor can be used to heat up water and methanol. The catalytic steam from the reforming methanol process yields a reformed composite. This composite has a 75 vol % of H_2, and 25 vol % CO_2. This composite may also contain residual methanol and CO [5].

$$CH_3OH + H_2O \rightarrow 3H_2 + CO_2$$
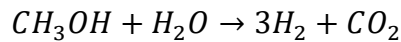
Equation 4:Endothermic reaction

$$2CH_3OH + 3O_2 \rightarrow 2CO_2 + 4H_2O$$
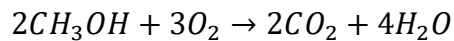
Equation 5: Exothermic reaction

$$2H_2 + O_2 \rightarrow 2H_2O$$
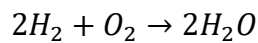
Equation 6: By product of the Exothermic reaction

History of fuel cells

The original concept of a fuel cell was first conceived by a Welshmen, Sir William Grove, in 1802 he devised a simple electrochemical cell using oxygen that was able to deliver a small electrics shock. This device had a carbon anode with a nitric acid electrolyte. However, he never published the findings from this experiment. The original device was called a Grove cell. Sir William Grove in 1838 teamed up with a Christian Friedrich Schonbein, German scientist. They were exploring the idea of that if water could be split into its constituent elements by an electrical current, then the process could be reversed, and hydrogen and oxygen used to generate a current. Grove's letter on the subject was published in *The London and Edinburgh Philosophical Magazine and Journal of Science* in December 1838, Schonbein's in 1839 and in consequence Grove is now considered the father of the fuel cell [6]. The original fuel cell called for a diluted Sulfuric acid as the electrolyte, zinc as the anode, and platinum as the cathode in a porous ceramic pot at room temperature. Walther Nerst, a German, produced the first ceramic fuel cells with the use of a solid oxide electrolytes at room temperature in 1899. Emil Baur and H. Preis produced the first solid

oxide fuel cell at 1000 degrees Celsius. These two individuals have shown the Nerst Mass and other materials that have zirconia-based material have a significant ionic conduction at such high temperatures. The Nerst Mass is a compound of 85 percent zirconia and 15 percent yttria [7].
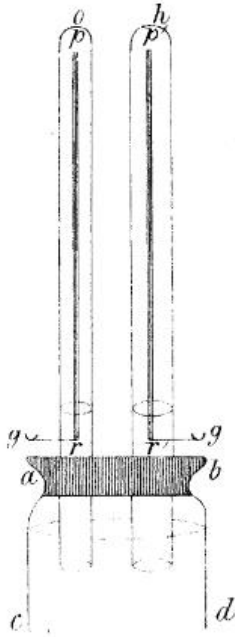
[8] Adapted from Solid Oxide Fuel Cells

Figure 4: Original fuel cell design

Modern day usages of fuel cells

In modern day, research for a fuel cell is mainly for production in either a transportation application or a stationary power source. Currently the United States government's Department of Transportation has given two different agencies that are in the Low and No-Emission (LoNo) Vehicle Deployment Program. One of these awards were given to the SunLine Transit Agency in California to construct a new maintenance facility for fuel cell buses and a learning center for staff on the new form of technology. This award was worth $1.5 million. The other award was given to the Stark Area Regional Transit Authority (SARTA) in Ohio to increase the amount of fuel cell buses. This award was worth $4 million. The United States Department of Defense has also

awarded the $3.46 million in the Small Business Innovation Research (SBIR) to fund four different projects relating to fuel cells. Also, the National Aeronautics and Space Administration (NASA) has funded the Fostering Ultra-Efficient Low Emitting Aviation Power (FUELEAP) group to develop a fuel cell that can generate power for an electronically propelled aviation sized aircraft. This award was almost $1 million [9].
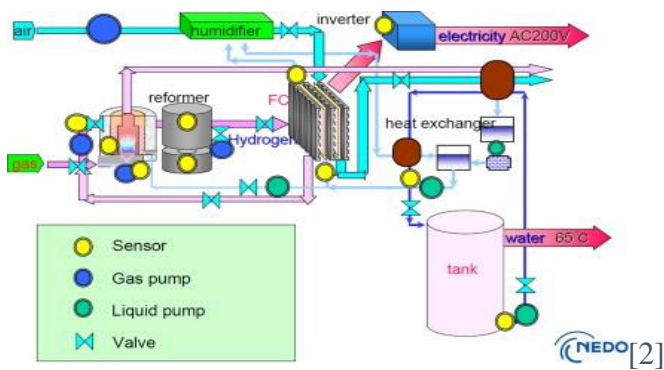
Adapted from *Chapter 2 - Fuel Cells and the Challenges Ahead*

Figure 5: Modern version of a fuel cell

Transportation application

        There are multiple different major automotive manufacturers that have a fuel cell vehicle that is in development, testing, or for lease right now. However, automotive manufactures are not the only ones incorporating fuel cells into production of transportation applications. Fuel cells are also being developed into buses, locomotives, airplanes, scooters, and golf carts. Fuel cells that use hydrogen as their fuel source produce a zero emission as a product and are much more efficient than battery powered or combustion engines. BMW and Delphi Automotive group have come out with a vehicle that has a solid oxide fuel cell to be used as an auxiliary power unit. This fuel cell produces enough energy to power its mechanically driven sub-systems, such as air conditioning and water pumps or even could run the vehicle while at idle. BMW will develop hydrogen fueled FC forklift trucks, deploying about 2,000 in the company's own facilities prior to marketing them to other users. Daimler-Benz is a part owner of Ballard and partners with Ford in development of a fuel

cell vehicle. Daimler has committed $725 million into their partnerships with Ballard and Ford for development. Meanwhile Volkswagen has introduced a fuel cell powered car that is a zero-emission vehicle. This vehicle is called the Bora HyMotion and is based on the Jetta platform. The HyMotion has a fuel cell engine that runs on hydrogen and has a power output of 75-kilowatts [10].

Stationary Power

Apple has recently revealed that their new Apple campus in Cupertino, California, will be the most energy efficient building of its kind. This building will be completely powered by renewable energy. This will be mainly possible due to two renewable technologies, a 4-megawatt biogas fuel cell and a 16-megawatts rooftop solar cells. When additional energy is needed it will come from a 130-megawatts solar project in Monterey County. This is due to Apple's power purchase agreement with First Solar. The site is designed as a microgrid—which allows Apple to disconnect from the local grid and power the campus autonomously when grid power goes down, providing energy resiliency [11]. While Morgan Stanley have announced in partnership with Bloom Energy the completion of a fuel cell project in their global headquarters in New York City's Time Square neighborhood. This 750-kilowatt fuel cell will be able to provide about 6 million kilowatts of clean energy each year. But this is not the only fuel cell device that Morgan Stanley has installed, the first system was installed in their Purchase, New York headquarters [12]. Ikea have contracted Sunnyvale-based Bloom Energy to install two fuel cell systems to their retail stores. One was placed in the Costa Mesa retail store which is 308,000 square feet on 24 acres. This is a 300-kilowatt fuel cell system that can produce about 2.5 million kilowatts of clean energy per year. This fuel cell can reduce the carbon dioxide emission by 1,315 tons, which is equivalent to 278 car's emission or 194 homes. The other was placed in the Covina retail store which is 325,000 square feet on 12.5 acres. This is a 200-kilowatt fuel cell system that can produce about 1.67 million kilowatts of clean energy per year. This fuel cell can reduce the carbon dioxide

emission by 877 tons, which is equivalent to 185 car's emission or 130 homes [13]. Meanwhile, Legrand North America, the parent company of Wiremold, which specializes in wire and cable management, have recently installed a new 500-kilowatt Solid Oxide Fuel Cell to power the 263,000 square feet campus in West Hartford, Connecticut. This is expected 88 percent of the entire campus's power. It is expected to save approximately $2.4 million in energy costs over the first 10 years of production [14].

Future of Fuel Cells

Like all new forms of technology, there is a continuous need for improvement of challenges that arise. One of these challenges that are being investigated is to improve the microstructure and material properties that can help reduce the operating temperature of the fuel cell. This would make the cost per cell more effective and make the thermodynamic efficiencies increase. This increase in thermodynamic efficiencies produces a longer lifetime and have quicker start up times. Currently, there are many approaches to solve this challenge like nanostructure thin film fuel cells, thick film fuel cells, strained engineered materials, etc. Another challenge on which researchers are working hard is to reduce the cost of production, storage, and transportation of hydrogen. Researchers are trying to develop proper infrastructure that will help to rectify these problems. The production of hydrogen through electrolysis and steam methane reforming on wide scale will help to reduce the cost of hydrogen. Along cost effective hydrogen production, researchers are working on cost effective storage [15, 16].

Over the next couple of years, Europe, Japan, and the United States have a unique style and approach in implementing and administering its fuel cells policies and programs. Japan has created three different entities: METI, NEDO, and AIST. METI oversees the overall fuel cell R&D program and entrusts day-to-day management to the NEDO. NEDO works in tandem with the

AIST, the National Institute of Advanced Industrial Science and Technology. AIST is Japan's largest public research organization with around 2400 researchers, comprising more than 40 autonomous research units under METI. AIST participates in NEDO's fuel cell R&D projects and works in collaboration with industrial participants. It also provides policy and programmatic inputs to METI. The three entities and their work are coherent, focused, and consistent.

Moreover, the United States has duplicative fuel cell programs. Two different programs have been implemented under two different budgets in two different DOE components. DOE's Office of Fossil Energy (FE) started a fuel cell program in the 1970s and supported R&D on PAFCs, MCFCs, and SOFCs. DOE's Office of Energy Efficiency and Renewable Energy (EERE) started PEMFC R&D in 2003 and gradually expanded its R&D activities to include some SOFCs and other fuel cell types. Historically, the dual approach has been justified by the fact that FE and EERE have two different jurisdictions; FE administers fossil fuel and PAFC, MCFC, and SOFC R&D because those fuel cells use fossil fuels; EERE administers renewable energy and PEMFC R&D because PEMFC uses hydrogen.

European R&D suffers from fragmentation among EC FP and individual European governments. Fragmentation prevented Europe from fulfilling its research and innovation potential, at a huge cost to Europeans as taxpayers, consumers, and citizens. Starting in 2000, Europe focused on overcoming the problem of fragmentation and launched a revolutionary policy to coordinate activities in 2007 [15].

Types of Fuel Cell

Over the years there have been five different fuel cells that have been studied. The difference between these types of fuel cells is mainly due to their electrolyte layer. These five fuel

cells are: phosphoric acid fuel cell, polymer electrolyte membrane fuel cell, alkaline fuel cell, molten carbonate fuel cell, and solid oxide fuel cell.

Phosphoric acid fuel cell

Phosphoric acid fuel cells, also known as high temperature proton exchange membrane fuel cell, uses a platinum catalyst and the phosphoric acid layer is where the proton exchange takes place. Phosphoric acid fuel cells typically take place at a temperature of 100-200 degrees Celsius. in recent years of research for commercializing the phosphoric acid fuel cells, there have been multiple different nano-porous polymers were explored for their applications. One of the best membranes discovered thus far is Polybenzimidazole. This membrane is suitable due to its stability in mechanical, thermal, and chemical properties. However, polybenzimidazole does not move protons nor electrons but do require a proton conductivity to absorb phosphoric acid. When polybenzimidazole absorbs too much phosphoric acid, it will start to decay. To accommodate the acid capacity as well the mechanical properties are to fill the inorganic with nanoparticles with a metal catalyst. This will allow the fuel to reach a higher power density. The typical stacking size is 5-400 kW of power with a liquid phosphoric acid fuel cell while with a polymer membrane is <10 kW of power with electrical efficiency of 40 %. The plans of applications are to use it in a distributed generation. The advantages and disadvantages are about equal for the phosphoric acid fuel cells. The advantages are they are suitable for combined heat and power and an increased tolerance to fuel impurities. While the disadvantages are the catalyst are expensive, has a long start up time and have a higher sulfur sensitivity [17, 18].

Polymer electrolyte membrane fuel cell

Polymer electrolyte membrane fuel cell is a promising alternative power source for multiple applications. This is due to the low operating temperatures, approximately 60-80 degrees Celsius. The most critical component of the polymer electrolyte membrane fuel cell is the

membrane electrode assembly. This is the component where the electrochemical reaction and conversion takes place. There are two current ways of preparing the membrane electrode assembly, by gas diffusion electron and the catalyst coated membrane. In the catalyst coated membrane method is directly applied on both sides of the polymer electrolyte. The gas diffusion electrode is hot pressed to the catalyst coated membrane electrode assembly prior to the assembly of the cell hardware. In current studies the gas diffusion electrode methods are producing a better cell performance [19, 20, 21]. Currently the most common form of electrolyte being used in the polymer electrolyte membrane fuel cell is Perfluorosulfonic acid. The typical stacking size is <1-100 kW of power with the electrical efficiency of 60% with direct hydrogen or 40% with a reformed fuel. The plans of applications are to use it in production of backup or portable power, distributed generation, transportation, and specialty vehicles. The present advantages of the Polymer Electrolyte Membrane Fuel Cells out way the disadvantages. The advantages are that the Solid electrolyte reduces corrosion and the electrolyte problems, low operating temperatures, and have a quick start-up. While the disadvantages are that the catalysts are expensive and are sensitive to any fuel impurities [18].

Alkaline fuel cell

Alkaline fuel cell was the first type of fuel cell to be placed into practicality. Alkaline fuel cell generates their electricity from hydrogen. Alkaline fuel cell was the basis for the vehicular applications of fuel cells. They were initially placed into farm tractors in the 1950s, then into the Austin A40 in the early 1970s, and even today in the ZEVCO company. However, in recent times the alkaline fuel cells research has been overshadowed because of other technologies and other kinds of fuel cells. The alkaline fuel cell was initially created for space applications to create electrical power for critical equipment. They were designed to provide constant power in a small space and weigh. Current performance data suggest that an alkaline fuel cell with an operating gas

pressure of 200 psi and at about 150 degrees Celsius with 50 weight% of potassium hydroxide electrolyte have reported current densities up to 9 A/cm^2 at approximately 0.7 V. While the aqueous potassium hydroxide soaked in a porous matrix is typical for the electrolyte, an alkaline polymer membrane is also typical. The typical stacking size is 1-100 kW of power with the electrical efficiency of 60%. The plans of applications are to use in the military, space, backup power, and transportation. The advantages and disadvantages are about equal for the Alkaline Fuel Cells. The advantages are they have a wider range of stable materials (which mean lower cost), low temperature, and quick start up. While the disadvantages are that they are sensitive to Carbon Dioxide in fuels and air and the electrolyte management and conductivity [18, 22].

Molten carbonate fuel cell

The molten carbonate fuel cells recently have attracted attention by researchers. This is due to its fuel flexibility, high efficiency, and low pollutants emission. The standard operating temperatures of the molten carbonate fuel cells are high compared to other fuel cells, around 500-600 degrees Celsius. This high temperature helps the reaction rate for its cheaper catalysts. Also, with these high temperatures, the high temperature exhaust gas can be integrated into gas turbines, Rankine cycle, or even the organic Rankine cycle. In one study, the molten carbonate fuel cell was able to produce an overall efficiency of 71.71% and an electrical efficiency of 42.28%. The most common electrolyte that is used for a Molten Carbonate Fuel Cell is either a molten lithium layer, sodium, or potassium carbonate soaked in a porous matrix. The typical stacking size is 300kW-3MW of power with electrical efficiency of 50%. The plans of applications are to use it as electric utility and its distributed generation. The advantages of molten carbonate fuel cells are the high efficiency, fuel flexibility, suitable for combined heat and power, and can be coupled with gas turbine cycles. While the disadvantages are it has high temperature corrosion and breakdown of the cell components, long start up time, and low power density [18, 23].

Solid oxide fuel cell

Solid oxide fuel cells have become the most promising power generation methods. This is mainly due to the high efficiency, nearly completely clean power generation, complete silent operation, and can be coupled with a turbine cycle. Some of the electrochemical models have momentum and heat transport showing a valuable method to study micro tubular solid oxide fuel cells. The impact of different cell sizes on the performance can provide an idea for the cell size design. Also, this impact can help understand how flow changes on internal current flow. But on the contrast, the flow change will alter the consumption rate of a single cell will change. In solid oxide fuel cells, the hydrogen is oxidized in the anode, which makes both hydrogen and steam exist in the anode. When the fuel consumption rate is too high, the amount of steam will be too high, which makes the anode have a large concentration polarization. The most common electrolyte for a solid oxide fuel cell is Yttria Stabilized with high operating temperatures of 500-1,000 degrees Celsius.

The main feature of the solid oxide fuel cell is the high energy conversion efficiency. Within the last couple of years of research, the efficiency of the solid oxide fuel cell has been increasing. In the last couple of years, the electrical efficiency at rated power of the solid oxide fuel cell has increased from 40 percent to 60 percent. While the CHP, combined heat and power, energy efficiency for the solid oxide fuel cell has increased from 85 percent to 90 percent. Not only has the efficiency but many other factors have been improved in the last couple of years. For instance, the factory cost of production from 1,300-4,500 to 1,000-2,000 $/kw; the degradation with cycling from <0.7 to <0.3 %/1,000 hours; and the time until there is less than 20 percent of net power degradation has gone from 30,000 hours (about 3.5 years) to 40,000 hours (about 4.5 years) [18, 23, 24] .

Zirconia, zirconium IV oxide, is a compound that can have three different polymorphic forms. These three polymorphic forms are monoclinic, tetragonal, and a face centered cubic. Pure zirconia at room temperature is a monoclinic crystal, but when heating up to between 1,000-2,000 degrees Celsius the zirconia transforms to its tetragonal phase. Once in this tetragonal phase the volume of the pure zirconia decreases in size. This volume shrinkage is about 3-10 %. Also, the transforming from the monoclinic to tetragonal phase leads to a residual stresses and cracking. The transition from tetragonal phase to the face centered cubic phase happens when the temperature is higher than 2000 degrees Celsius. In addition, the tetragonal-face centered cubic transformation induces another volume shrinkage. From these constant volume reductions pure zirconia cannot be sintered. But when transforming back from a face centered cubic to the tetragonal phase the pure zirconia the volume increases, has higher stress, and has a higher rate cracking due to the cooling from a high temperature. To prevent the volume change during these phase changes the zirconia must be stabilized with an oxide for the tetragonal and face centered cubic phases. Two of the most common oxides that are used are yttria, also known as yttrium oxide, or magnesium oxide [25].

Pure yttria, or yttrium oxide, at room temperature is a body-centered cubic material with bixbyite or cubit C-structure, but when heating up to just under 2,400 degrees Celsius the phase form transforms to a hexagonal phase. Just past this transformation temperature is the melting point of pure yttria. It is shown that a partial pressure of oxygen is a critical factor in producing a low level of defect absorption. The main defect of pure yttria is its oxygen vacancies. When placed in a reducing atmosphere with very high temperature, above 1,700 degrees Celsius pure yttria is transformed from a pure white color to a black color. This black yttria has a very high absorption

which can be visible. At about 900 degrees Celsius absorption increases even more. This is most

likely due to a higher concentration of the oxygen vacancies [26].

First Law of Thermodynamics

To fully understand the thermal efficiency of fuel cell the thermodynamics of the fuel cell. The current fuel cells continuously have a production of electricity and heat. The fuel cells are operating over a time, Δt, in which fuel and oxidants are added to continuously added to continue the electrical potential. If there is current is allowed, the charge carriers migrate from higher to lower electrical and chemical potentials across the cell. Therefore, the change in Gibbs free energy, can be shown by the following equation, of reaction drives the electrical current.

$$\Delta G = \Delta E + P\Delta V - T\Delta S$$

Equation 7: Gibbs Free Equation

The Gibbs free energy (G) can be shown as well as energy (E), pressure (P), volume (V), temperature (T), enthalpy (S) [27]. The First Law of Thermodynamics states the conservation of energy, no form of energy cannot be crated or destroyed in an isolated system. However, the First Law of Thermodynamics cannot indicate how the cell can perform while working in an isothermal environment. According to this law the fuel cells can be assumed as reversable. The first Law of Thermodynamics for a reversible fuel cell can be expressed by the following equation. Where heat (q), work (w), and electrical work ($w_{electical}$) [28].

$$\Delta E = q + w = q + w_{electical} - P\Delta V$$

Equation 8: First Law of thermodynamics

Taking this equation and plugging into the Gibbs free energy equation, it simplifies down to the following equation. However, since the operation of a fuel cell can be reversible. Which means the heat is equal to the temperature times the change in enthalpy.

$$\Delta G = T\Delta S + w_{electical} - P\Delta V + P\Delta V - T\Delta S$$

Equation 9: Plugging the First Law of thermodynamics into the Gibbs free Equation

$$\Delta G = w_{electical}$$

Equation 10: Plugging the First Law of thermodynamics into the Gibbs free Equation simplified

This simplified Gibbs equation shows that the Gibbs free energy of reaction is equal to the electrical work of the system. The electrical work (J) in an open system operated continuously over a given time, Δt, where reactants (moles/second) are added, and products removed to maintain the electrical potential is given for hydrogen–oxygen reaction the following equations

$$m_{H_2\ utilized} \Delta G \Delta t = m_{H_2} w_{eletrical} \Delta t = W_{electrical}$$

Equation 11: Electrical Work

$$m_{H_2\ inlet} w_{rev} = m_{H_2\ inlet} \Delta G^0 \Delta t = W_{rev}$$

Equation 12: Reversible Work

Where m_{H_2} is the flow rate of hydrogen for the H_2/O_2 reactions, $m_{H_2\ inlet}$ is the flow rate of hydrogen fuel into the system. These two are important in the determining Exergetic efficiency. The Exergetic efficiency is the total ratio of electrical work and the reversible work, which is represented as ζ.

$$\zeta = \frac{W_{electrical}}{W_{rev}} = \frac{m_{H_2\ utilized} \Delta G}{m_{H_2\ inlet} \Delta G^0} = \mu_F \frac{\Delta G}{\Delta G^0}$$

Equation 13: Exergetic efficiency formula

Using the equation for the reversible work, one can calculate the maximum thermal efficiency (maximum work for given energy input) of a fuel cell or fuel cell hybrid (fuel cell and heat engine) system for the H_2 oxidation reaction, where ΔH^0 is the reaction enthalpy for hydrogen direct oxidation (J/mole) at standard temperature and pressure and where the inlet hydrogen is completely utilized in the fuel cell:

$$\eta_{th\ max} = \frac{\Delta G^0}{\Delta H^0}$$

Equation 14: Equation for maximum thermal efficiency

While the actual thermal efficiency can be written as [27]

$$\eta = \eta_{th\,max}(\zeta)$$

Equation 15: Equation for Actual thermal efficiency

Pulsed Laser Deposition

Pulsed laser deposition is one of the simpler techniques in creating thin films. The pulsed laser deposition technique uses a pulsed laser that irradiated the surface of the target. The targeted is the desired element or compound as a thin film. A pulsed laser is first shot at mirrors to align the pulsed laser to a fine point. The last mirror passes the laser through a suitable window on the side of the vacuum chamber. When the focused and sufficiently intense laser beam is focused on the desired target leading to the ejection of material. The density and the excitation degree of the material is very high, leading to the formation of a plume. This plume expands perpendicular to the surface of the target. A substrate is placed a short distance away and parallel to the surface of the target. This substrate is in the path of the plume and a fraction of the species will adhere to the surface of the substrate. Over time, the plume continues to be in contact with the substrate creating a film [29].
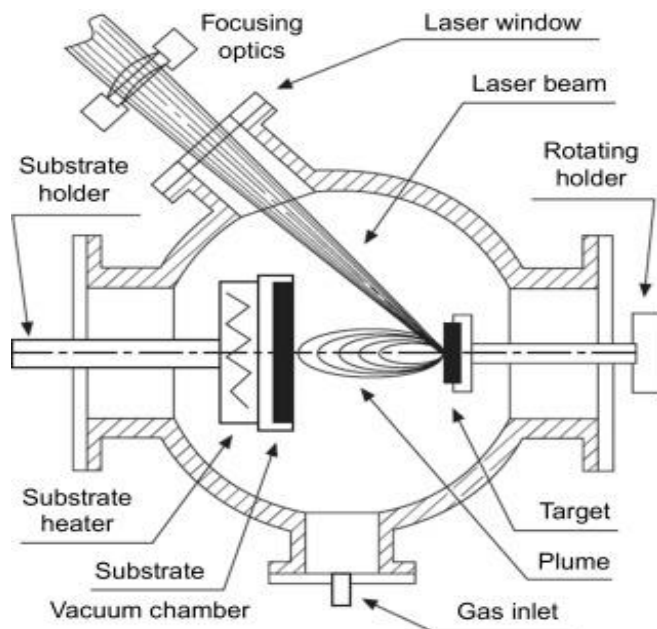
[29] Adapted from Chapter 14 - Production of Biomaterial Coatings by Laser-Assisted Processes

Figure 6: Image of pulsed laser deposition process

The pulsed laser deposition process has been found to have advantages when compared to other types of thin film depositions devices. One of the main advantages is when creating the films, the same chemical structure of the target will be the same as the film. Another advantage is this process is extremely flexible to different compounds. Another is the use of a carousel. In many pulsed laser deposition chambers, there are carousels that hold multiple different targets. This is useful because it saves the time from bringing the chamber back to atmospheric pressure, changing the targets, then repumping back down to ultrahigh vacuum.

The pulsed laser deposition process has only two main disadvantages. The first is the particulates deposited onto the film. Two main cases for particle formation during laser evaporation are the breakaway of surface defects under thermal shock and splashing of liquid material due to superheating of subsurface layers. The other problem is nonuniformity over a large are of the plume. The plasma plume that is created has a very narrow angular distribution that comes from the target. But these disadvantages are currently being worked on for the next generation of pulsed laser deposition machines [30].

Ellipsometer

Ellipsometry is a very sensitive, nondestructive, nonperturbing technique that uses the change in polarization of light upon reflection for characterization of surfaces, interfaces, and thin films. The main principle of the ellipsometer is to change the polarization of the light that is being reflected off the sample's surface by measuring by taking the amplitude ratios of two perpendicularly polarizing beams. For an isotropic, non-absorbing layers the measurement is usually a laser, or some type of single wavelength. When the measured the refractive index, absorption coefficient, and thickness of the layers. The ellipsometer can measure complex and multiple layers [31]. Since the 1960s, the ellipsometry has constantly been improved its sensitivity

to the nanometer scale. The widespread usage of an ellipsometer increased the production and accuracy of the thickness of the dielectrics, semiconductors, metals, superconductors, organics, biological coatings, and composites of materials [32].
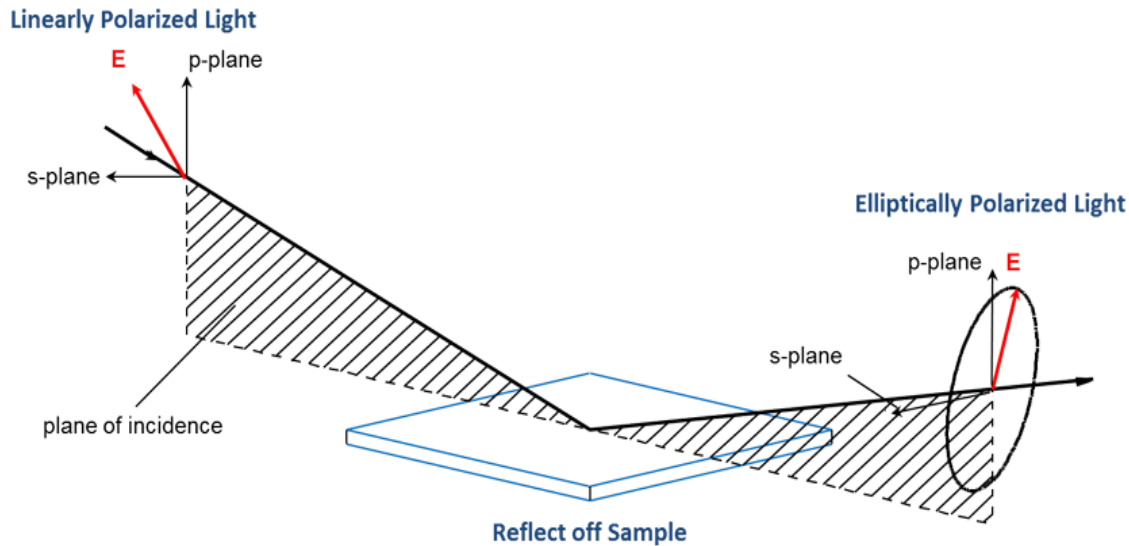
[32]

Adapted from "What Is Ellipsometry?"

Figure 7: Schematic of an Ellipsometer

Four-point probe

The purpose of a Four-point probe is to measure the resistivity of a material. These materials can be either a bulk or thin films layers. These different types of layers are expressed by two different equations. The Four-point probe is compiled of four equally spaced metal tips, usually made up of tungsten, with very fine radiuses. Typically, these distances between each of the probes, s, are about 1 mm apart from each other. Each tip is supported by springs on the ends to minimize the sample damage while taking measurements. Two of these probes, usually the outer two probes, have the current going from the probes to the layers and but in opposite charges. The other two probes have a voltmeter connected across them [33].

[33]
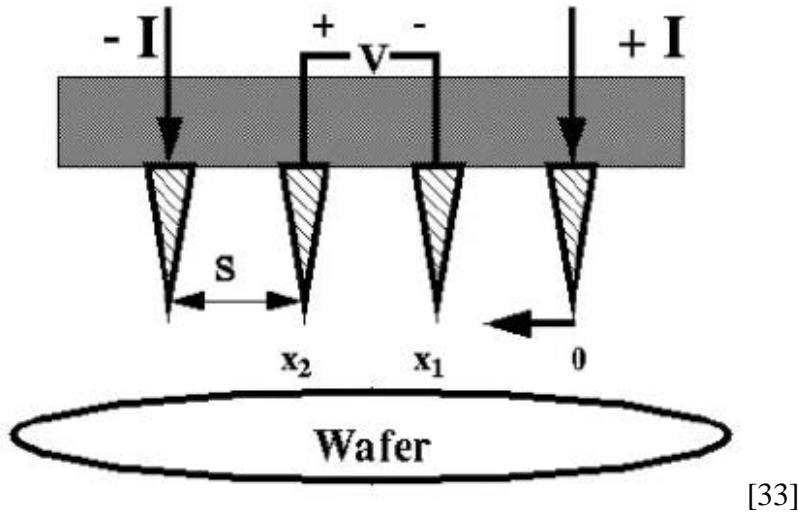
Figure 8: Schematic of 4-point probe

Bulk Layer

Typically, a bulk layer is defined as a layer that has a thickness that is much greater than the distance between two probes, s. It is assumed that the probes' radiuses are very small, in calculations infinitesimally small, and the bulk layer has a large dimension compared to the radiuses. The expression for the bulk resistivity is shown by the next equation and the conductivity is the one after:

$$\rho = \frac{2\pi s V}{I}$$

Equation 16: Bulk resistivity equation

$$\sigma = \frac{1}{\rho}$$

Equation 17: Conductivity equation

Where ρ is the bulk resistivity, s is the distance between the probes, V is the voltage read from the voltmeter connected to two of the probes, and I is the current passed through the other two probes.

Thin layer

Unlike the bulk layer, the thin layer is defined as a layer that has a thickness that is much smaller than the distance between two probes, s. Also, the thin layer, requires the thickness of the

22

layer to determine the resistivity. Like before, it is assumed that the probes' radiuses are very small, in calculations infinitesimally small, and the bulk layer has a large dimension compared to the radiuses. The equation for the conductivity remains the same while the expression for the thin resistivity is shown by the next equation where t is the thickness of the layer [34]:

$$\rho = \frac{\pi t}{\ln(2)} * \frac{V}{I}$$

Equation 18: Thin Film resistivity equation

Scanning Electron Microscope

A Scanning Electron Microscope is a type of microscope in which uses a fine probe of electrons to create an image. These probes are typically up to 40 keV. The probe is focused on the desired material and then is scanned in a pattern of parallel lines. From the contact with the electrons and the material, there are multiple different types of signals that are produced. These electrons are collected from the impact of the incident electrons are used to form the image of the surface of the material. The secondary electrons, usually in a scaling of a few tens of eVs, are usually much lower than the incident electrons. These electrons are then collected and can be used to find out the X-ray characteristics of the material. currently there is one main problem of obtaining a high-resolution image. There are two main ways to acquire a high-resolution. The first is to decrease the magnification on the material. At high magnification, the image's resolution is about the same of the width of the probe of the electrons. It is limited by a few key parameters: aberrations of the lenses, especially the objective lens because it works at large convergence angles, the brightness of the electron source, and the interaction volume, especially when the samples are not very thin. The second is the conservation of the brightness in the microscope column. The low resolutions that appear is due to the electron flux becomes too low in the probe [35].

To create the various yttrium stabilized zirconium targets needed for the depositions to create the electrolyte layer using the Pulsed Laser Deposition method, the materials needed are zirconium (IV) oxide and yttrium III oxide powders. The zirconium (IV) oxide being used is from Sigma Aldrich and has a 99% trace metal basis with a powder size of about 5 μm. The yttrium III oxide being used is also from Sigma Aldrich and has a 99.99% trace metals basis. The zirconium (IV) oxide and yttrium III oxide were ground separately at first for thirty minutes each. This was done to create an overall uniformity in the powder size within each powder. The amount needed from each powder to create each target was measured out, mixed, and re-grounded together for another thirty minutes. The concentrations that will be created and studied are the following: $(ZrO_2)_{0.99} \cdot (Y_2O_3)_{0.01}$, $(ZrO_2)_{0.97} \cdot (Y_2O_3)_{0.03}$, $(ZrO_2)_{0.95} \cdot (Y_2O_3)_{0.05}$, $(ZrO_2)_{0.93} \cdot (Y_2O_3)_{0.07}$, $(ZrO_2)_{0.91} \cdot (Y_2O_3)_{0.09}$, and $(ZrO_2)_{0.90} \cdot (Y_2O_3)_{0.10}$.
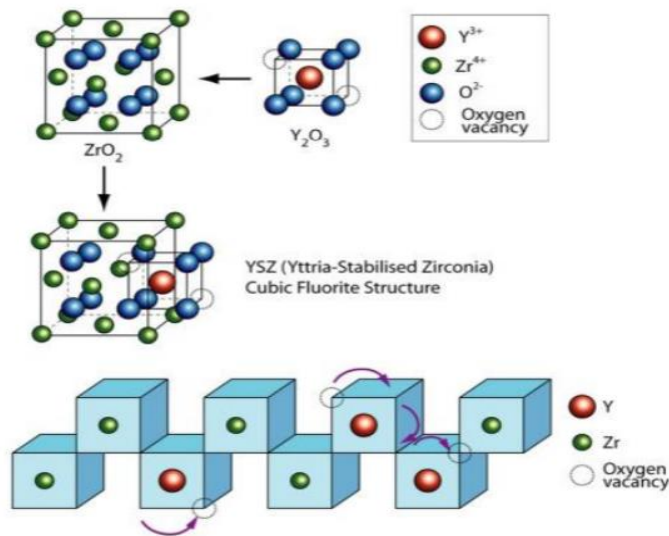
[38]

Figure 9: Doping and vacancy transport in YSZ

The mixed and crushed powder was then created into cylindrical target. This was done by placing the powder into a hydraulic press for a total of thirty minutes at an applied load of 10,000 kilograms. These targets were 0.3175 cm tall and 2.54 cm in diameter.

	$(ZrO_2)_{0.99} \cdot (Y_2O_3)_{0.01}$,	$(ZrO_2)_{0.97} \cdot (Y_2O_3)_{0.03}$	$(ZrO_2)_{0.95} \cdot (Y_2O_3)_{0.05}$	$(ZrO_2)_{0.93} \cdot (Y_2O_3)_{0.07}$	$(ZrO_2)_{0.92} \cdot (Y_2O_3)_{0.08}$	$(ZrO_2)_{0.90} \cdot (Y_2O_3)_{0.10}$
ZrO_2	8.2905	7.9910	7.7012	7.4204	7.2833	7.0155
Y_2O_3	0.1535	0.4530	0.7428	1.0236	1.1607	1.4285

Table 1: Grams of each compound in each target

These measurements were calculated first by calculating the volume of the cylinder that will be used. Next the percent of each compound will be needed to calculate the combined density of the mixture.

$$V = \pi r^2 h$$

Equation 19: Volume of a cylinder

$$\%_{ZrO_2 \ in \ mixture} = \left(\frac{M_{ZrO_2}}{M_{ZrO_2} + M_{Y_2O_3}} \right) * 100\%$$

Equation 20: Percent ZrO_2 in mixture

$$\%_{Y_2O_3 \ in \ mixture} = \left(\frac{M_{Y_2O_3}}{M_{ZrO_2} + M_{Y_2O_3}} \right) * 100\%$$

Equation 21: Percent Y_2O_3 in mixture

$$\rho_{(ZrO_2)_{1-x} \cdot (Y_2O_3)_x} = \left(\left(\frac{\%_{ZrO_2 \ in \ mixture}}{100} \right) * \rho_{ZrO_2} \right) + \left(\left(\frac{\%_{Y_2O_3 \ in \ mixture}}{100} \right) * \rho_{Y_2O_3} \right)$$

Equation 22: Density of $(ZrO_2)_{1-x} \cdot (Y_2O_3)_x$

From this new density, the amount each target weighs can be calculated. The grams needed for each composition needed can be calculated to the wanted concentrations.

$$m_{(ZrO_2)_{1-x}\cdot(Y_2O_3)_x} = V * \rho_{(ZrO_2)_{1-x}\cdot(Y_2O_3)_x}$$

Equation 23: Mass of $(ZrO_2)_{1-x} \cdot (Y_2O_3)_x$ *targets*

$$mol_{ZrO_2} = \frac{m_{ZrO_2}}{M_{ZrO_2}}$$

Equation 24: mol of ZrO_2

$$mol_{Y_2O_3} = \frac{m_{Y_2O_3}}{M_{Y_2O_3}}$$

Equation 25: mol of Y_2O_3

$$x = \frac{mol_{Y_2O_3}}{mol_{ZrO_2}+mol_{Y_2O_3}}$$

Equation 26: Concentration of the compound

Finally, before being placed in the Pulsed Laser Deposition chamber, each of these targets were placed into a high temperature furnace. This furnace was set to the following parameters: 25 minutes ramping rate up at 10 degrees Celsius per minute, holding at a constant 250 degrees Celsius for sixty minutes, and then 25 minutes ramping rate downward at 10 degrees Celsius per minute.

Pulsed Laser Deposition

As previously stated, the method of producing the electrolyte layer is being investigated. With this process, subtle changes in the programing of the laser can create vast differences in the thin film layers. For instance, peak voltage, base pressure, laser pulses frequency, substrate temperature, distance from the target to the substrate, length of the laser pulsing, laser energy, targets, substrates, etcetera. In this experiment, these subtle changes in the programing of the laser are being explored. Specifically, this experiment will be manipulating the laser energy and comparing the differences if the electrolyte layer. The laser that used in this experiment is a 248-nanometer wavelength ultraviolet Krypton Fluoride Excimer Laser (TuiLaser) from PVD products. The targets were created by the previously discussed method, but the substrates being used are prefabricated substrates by MTI corporation. The substrates that are being used are

Polished Zr, Polished Al_2O_3, and Polished Silicon. The following table shows the parameters used during the Pulsed Laser Deposition method deposition of the electrolyte layer.

High Voltage	20,000-30,000 V
Base Pressure	5.0 E -6 Torr
Frequency	5 Hz
Substrate Temperature	20 Degrees Celsius
Target Distance	6 cm
Substrate Temperature	20 Degrees Celsius
Target Distance	6 cm
Deposition Time	20 minutes
Laser Energy	100 mJ or 120 mJ
Laser Energy Density	1.188 J/cm^2 or 1425 J/cm^2
Shots	6,000
Target	$(ZrO_2)_{1-x} \cdot (Y_2O_3)_x$
Substrate	Polished Zr, Polished Al_2O_3, or Polished Si

Table 2: Parameters used for all Pulsed Laser Depositions

Ellipsometer

As previously stated, an ellipsometer is a tool that can measure a thickness of a film. This process is useful not only to determine the precision and accuracy of the thickness of a film, but also to use this data for later calculations. In this experiment the ellipsometer program that was used was a Gaertner Ellipsometer Program (LGEMP). In this program can calculate the thickness of four films deposited onto each other in the value of angstroms, however in this experiment there is one film that is being measured. The values that were entered into the program were 8000

Thickness 1, 1.915 for NF1, and 3.85, 3.9, and 3.88 for NS for Polished Zirconium, Polished Al_2O_3, and Polished Silicon, respectively. The value of Thickness 1 was pressed in, which means the values can be varied. The values of Thickness 2, Thickness 3, Thickness 4, NF2, NF3, and NF4 were 0. This is because there was only one layer that was deposited. The ellipsometer was used to measure the thickness for each layer at five different points. These points are defined by the following figure where 1 represents Corner 1, 2 represents Corner 2, 3 represents Corner 3, 4 represents Corner 4, and C represents Center. The resulting values are in Angstroms and for calculations these values will be converted to meters.
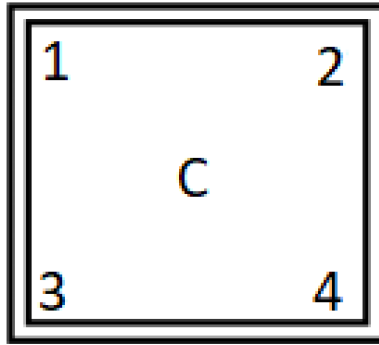
Figure 10: Ellipsometer and 4-point probe positioning

4-point probe

A four-point probe characterization was used to determine the sheet resistance of the deposited film. The sheet resistance was measured using a Jandel Model RM3 four-point positioning probe. The four-point probe was placed into 1 mA of current, the measurements were taken in $\Omega/\blacksquare$, and a low sensitivity. The probes were lowered onto the surface of the $(ZrO_2)_{1-x} \cdot (Y_2O_3)_x$ film, making sure not to fully penetrate and ruin the layer to acquire the sheet resistance. The average sheet resistance was taken based off 100 measured points at the same position as the ellipsometer measures. These values are taken and later used to calculate the resistivity of the $(ZrO_2)_{1-x} \cdot (Y_2O_3)_x$ films.

Scanning Electron Microscope

The three objectives that were performed when using the Scanning Electron Microscope were as followed: 1) to observe the interface between the substrate and the deposited film, 2) to verify the thickness of the deposited film, and 3) to verify the deposited layer is even and does not have any protrusions or depressions. The images that are presented are taken from a JEOL 6400. Each sample was prepared by placing it in the proper sample holder. Then placing Copper tape to ground the sample to the sample holder.

Results
Ellipsometer

In the following tables the thin films are measured in angstroms and will be compared to 8,000 Angstroms. For the $(ZrO_2)_{1-x} \cdot (Y_2O_3)_x$ films on Polished Zirconium with 100 mJ of laser energy, the average thickness for each increasing concentration were 7850, 8175, 7650, 7812, 7539, and 8535 Angstroms, respectively. From this the overall thickness for all concentrations was 7927 Angstroms compared to 8,000 Angstroms. This has a percent difference of 0.916682%.

Position	$(ZrO_2)_{0.99}$ $\cdot (Y_2O_3)_{0.01}$	$(ZrO_2)_{0.97}$ $\cdot (Y_2O_3)_{0.03}$	$(ZrO_2)_{0.95}$ $\cdot (Y_2O_3)_{0.05}$	$(ZrO_2)_{0.93}$ $\cdot (Y_2O_3)_{0.07}$	$(ZrO_2)_{0.92}$ $\cdot (Y_2O_3)_{0.08}$	$(ZrO_2)_{0.90}$ $\cdot (Y_2O_3)_{0.10}$
Center	7846	6824	6974	8061	7199	9017
Corner 1	7840	8133	7677	7774	7455	8383
Corner 2	7854	8481	7034	8203	7951	9336
Corner 3	7854	8695	7254	7682	7998	8961
Corner 4	7855	8743	9312	7338	7093	6976

Table 3: Ellipsometer readings of 100 mJ onto Polished Zirconium in Angstroms

For the $(ZrO_2)_{1-x} \cdot (Y_2O_3)_x$ films on Polished Zirconium with 120 mJ of laser energy, the average thickness for each increasing concentration were 7887, 7849, 7936, 7905, 7907, and 7885 Angstroms, respectively. From this the overall thickness for all concentrations was 7895 Angstroms compared to 8,000 Angstroms. This has a percent difference of 1.32117%.

Position	$(ZrO_2)_{0.99}$ $\cdot (Y_2O_3)_{0.01}$	$(ZrO_2)_{0.97}$ $\cdot (Y_2O_3)_{0.03}$	$(ZrO_2)_{0.95}$ $\cdot (Y_2O_3)_{0.05}$	$(ZrO_2)_{0.93}$ $\cdot (Y_2O_3)_{0.07}$	$(ZrO_2)_{0.92}$ $\cdot (Y_2O_3)_{0.08}$	$(ZrO_2)_{0.90}$ $\cdot (Y_2O_3)_{0.10}$
Center	7889	7853	7961	7905	7903	7886
Corner 1	7872	7845	7850	7923	7918	7881
Corner 2	7886	7834	7965	7905	7909	7868
Corner 3	7888	7864	7962	7902	7919	7902
Corner 4	7900	7851	7943	7891	7887	7889

Table 4: Ellipsometer readings of 120 mJ onto Polished Zr in Angstroms

For the $(ZrO_2)_{1-x} \cdot (Y_2O_3)_x$ films on Polished Al_2O_3 with 100 mJ of laser energy, the average thickness for each increasing concentration were 8558, 8371, 8545, 8556, 8119, and 8561 Angstroms, respectively. From this the overall thickness for all concentrations was 8452 Angstroms compared to 8,000 Angstroms. This has a percent difference of 5.49477 %.

Position	$(ZrO_2)_{0.99}$ $\cdot (Y_2O_3)_{0.01}$	$(ZrO_2)_{0.97}$ $\cdot (Y_2O_3)_{0.03}$	$(ZrO_2)_{0.95}$ $\cdot (Y_2O_3)_{0.05}$	$(ZrO_2)_{0.93}$ $\cdot (Y_2O_3)_{0.07}$	$(ZrO_2)_{0.92}$ $\cdot (Y_2O_3)_{0.08}$	$(ZrO_2)_{0.90}$ $\cdot (Y_2O_3)_{0.10}$
Center	8560	8363	8556	8555	8108	8562
Corner 1	8550	8388	8556	8552	8157	8550
Corner 2	8560	8484	8544	8557	8145	8562
Corner 3	8559	8270	8532	8555	8094	8562
Corner 4	8562	8350	8535	8562	8089	8569

Table 5: Ellipsometer readings of 100 mJ onto Polished Al_2O_3 in Angstroms

For the $(ZrO_2)_{1-x} \cdot (Y_2O_3)_x$ films on Polished Al_2O_3 with 120 mJ of laser energy, the average thickness for each increasing concentration were 8550, 8579, 8585, 8553, 8549, and 8548 Angstroms, respectively. From this the overall thickness for all concentrations was 8560 Angstroms compared to 8,000 Angstroms. This has a percent difference of 6.76329%.

Position	$(ZrO_2)_{0.99}$ $\cdot (Y_2O_3)_{0.01}$	$(ZrO_2)_{0.97}$ $\cdot (Y_2O_3)_{0.03}$	$(ZrO_2)_{0.95}$ $\cdot (Y_2O_3)_{0.05}$	$(ZrO_2)_{0.93}$ $\cdot (Y_2O_3)_{0.07}$	$(ZrO_2)_{0.92}$ $\cdot (Y_2O_3)_{0.08}$	$(ZrO_2)_{0.90}$ $\cdot (Y_2O_3)_{0.10}$
Center	8551	8577	8582	8551	8549	8549
Corner 1	8543	8582	8572	8553	8549	8546
Corner 2	8549	8588	8585	8560	8542	8540
Corner 3	8549	8571	8585	8547	8550	8553
Corner 4	8554	8578	8603	8553	8552	8550

Table 6: Ellipsometer readings of 120 mJ onto Polished Al_2O_3 in Angstroms

For the $(ZrO_2)_{1-x} \cdot (Y_2O_3)_x$ films on Polished Silicon with 100 mJ of laser energy, the average thickness for each increasing concentration were 8228, 7851, 7856, 7841, 7812, and 7715 Angstroms, respectively. From this the overall thickness for all concentrations was 7884 Angstroms compared to 8,000 Angstroms. This has a percent difference of 1.46059%.

Position	$(ZrO_2)_{0.99}$ $\cdot (Y_2O_3)_{0.01}$	$(ZrO_2)_{0.97}$ $\cdot (Y_2O_3)_{0.03}$	$(ZrO_2)_{0.95}$ $\cdot (Y_2O_3)_{0.05}$	$(ZrO_2)_{0.93}$ $\cdot (Y_2O_3)_{0.07}$	$(ZrO_2)_{0.92}$ $\cdot (Y_2O_3)_{0.08}$	$(ZrO_2)_{0.90}$ $\cdot (Y_2O_3)_{0.10}$
Center	8236	7882	7852	7843	7816	7717
Corner 1	8236	7849	7906	7809	7852	7716
Corner 2	8211	7857	7805	7844	7808	7709
Corner 3	8103	7846	7864	7834	7807	7716
Corner 4	8352	7819	7855	7875	7779	7718

Table 7: Ellipsometer readings of 100 mJ onto Polished Silicon in Angstroms

For the $(ZrO_2)_{1-x} \cdot (Y_2O_3)_x$ films on Polished Silicon with 120 mJ of laser energy, the average thickness for each increasing concentration were 7850, 7842, 7770, 7872, 7832, and 7838 Angstroms, respectively. From this the overall thickness for all concentrations was 7834 Angstroms compared to 8,000 Angstroms. This has a percent difference of 2.09675%.

Position	$(ZrO_2)_{0.99}$ $\cdot (Y_2O_3)_{0.01}$	$(ZrO_2)_{0.97}$ $\cdot (Y_2O_3)_{0.03}$	$(ZrO_2)_{0.95}$ $\cdot (Y_2O_3)_{0.05}$	$(ZrO_2)_{0.93}$ $\cdot (Y_2O_3)_{0.07}$	$(ZrO_2)_{0.92}$ $\cdot (Y_2O_3)_{0.08}$	$(ZrO_2)_{0.90}$ $\cdot (Y_2O_3)_{0.10}$
Center	7853	7846	7770	7879	7835	7842
Corner 1	7845	7843	7798	7852	7838	7826
Corner 2	7834	7839	7764	7871	7837	7841
Corner 3	7864	7834	7768	7874	7821	7842
Corner 4	7852	7846	7750	7885	7830	7839

Table 8: Ellipsometer readings of 120 mJ onto Polished Silicon in Angstroms

Taking all the overall thickness from the Polished Zirconium, Polished Al_2O_3, and Polished Silicon from both 100 mJ and 120 mJ, the accuracy and precision of the Pulsed Laser Deposition can be determined. Taking the values of 7927, 7895, 8452, 8560, 7884, and 7834

Angstroms, the overall average of all the $(ZrO_2)_{1-x} \cdot (Y_2O_3)_x$ regardless of the substrate is 8092

Angstroms. Comparing this thickness to the ideal thickness of 8,000 Angstroms it has a 1.14343%

difference.

4-point probe and Resistivity

As the results show in the following tables, the four-point probe's show an overall

uniformity from one position to another for each of the concentrations on the Polished Zr, Al_2O_3,

and Si for the 100 mJ deposited layers. However, the tables that show the four-point probe's

results for the 120 mJ does show a wider range of values with more irregular data points compared

to the 100 mJ data points. With considering all the data, with the increasing concentration the

values decrease and then flattens out around $(ZrO_2)_{0.92} \cdot (Y_2O_3)_{0.08}$ and

$(ZrO_2)_{0.90} \cdot (Y_2O_3)_{0.10}$ for both the 100 mJ and the 120 mJ energy levels.

Position	$(ZrO_2)_{0.99}$ $\cdot (Y_2O_3)_{0.01}$	$(ZrO_2)_{0.97}$ $\cdot (Y_2O_3)_{0.03}$	$(ZrO_2)_{0.95}$ $\cdot (Y_2O_3)_{0.05}$	$(ZrO_2)_{0.93}$ $\cdot (Y_2O_3)_{0.07}$	$(ZrO_2)_{0.92}$ $\cdot (Y_2O_3)_{0.08}$	$(ZrO_2)_{0.90}$ $\cdot (Y_2O_3)_{0.10}$
Center	496.673	304.707	188.362	451.843	115.576	176.436
Corner 1	586.921	168.264	769.29	205.998	90.5574	281.974
Corner 2	219.144	411.269	372.428	161.576	279.785	165.1
Corner 3	397.727	218.894	650.323	171.793	132.417	120.2
Corner 4	281.987	201.038	23.0067	88.7473	66.9401	358.565

Table 9: Average Sheet Resistance of 100 mJ onto Polished Zirconium

Position	$(ZrO_2)_{0.99}$ $\cdot (Y_2O_3)_{0.01}$	$(ZrO_2)_{0.97}$ $\cdot (Y_2O_3)_{0.03}$	$(ZrO_2)_{0.95}$ $\cdot (Y_2O_3)_{0.05}$	$(ZrO_2)_{0.93}$ $\cdot (Y_2O_3)_{0.07}$	$(ZrO_2)_{0.92}$ $\cdot (Y_2O_3)_{0.08}$	$(ZrO_2)_{0.90}$ $\cdot (Y_2O_3)_{0.10}$
Center	424.233	556.079	271.199	212.57	169.512	308.465
Corner 1	379.476	276.709	112.585	97.6801	229.125	266.691
Corner 2	509.381	465.554	338.527	337.211	128.478	370.558
Corner 3	444.906	288.876	343.12	313.14	127.12	192.405
Corner 4	185.925	356.95	114.488	277.458	128.646	174.548

Table 10: Average Sheet Resistance of 120 mJ onto Polished Zirconium

Position	$(ZrO_2)_{0.99}$ $\cdot (Y_2O_3)_{0.01}$	$(ZrO_2)_{0.97}$ $\cdot (Y_2O_3)_{0.03}$	$(ZrO_2)_{0.95}$ $\cdot (Y_2O_3)_{0.05}$	$(ZrO_2)_{0.93}$ $\cdot (Y_2O_3)_{0.07}$	$(ZrO_2)_{0.92}$ $\cdot (Y_2O_3)_{0.08}$	$(ZrO_2)_{0.90}$ $\cdot (Y_2O_3)_{0.10}$
Center	748.566	734.954	605.999	618.838	514.867	555.196
Corner 1	713.555	720.004	632.184	590.661	559.69	500.189
Corner 2	704.24	565.573	665.6	535.148	561.655	668.662
Corner 3	734.936	987.019	617.222	584.286	550.99	571.818
Corner 4	717.748	721.639	619.046	588.343	478.42	623.503

Table 11: Average Sheet Resistance of 100 mJ onto Polished Al_2O_3

Position	$(ZrO_2)_{0.99}$ $\cdot (Y_2O_3)_{0.01}$	$(ZrO_2)_{0.97}$ $\cdot (Y_2O_3)_{0.03}$	$(ZrO_2)_{0.95}$ $\cdot (Y_2O_3)_{0.05}$	$(ZrO_2)_{0.93}$ $\cdot (Y_2O_3)_{0.07}$	$(ZrO_2)_{0.92}$ $\cdot (Y_2O_3)_{0.08}$	$(ZrO_2)_{0.90}$ $\cdot (Y_2O_3)_{0.10}$
Center	816.062	559.155	584.737	562.018	565.75	565.853
Corner 1	704.093	664.32	627.796	586.526	671.443	502.262
Corner 2	720.961	705.188	989.952	559.025	610.249	586.219
Corner 3	724.157	752.702	585.624	590.723	603.701	572.39
Corner 4	732.897	626.388	710.222	549.392	616.129	548.347

Table 12: Average Sheet Resistance of 120 mJ onto Polished Al_2O_3

Position	$(ZrO_2)_{0.99}$ $\cdot (Y_2O_3)_{0.01}$	$(ZrO_2)_{0.97}$ $\cdot (Y_2O_3)_{0.03}$	$(ZrO_2)_{0.95}$ $\cdot (Y_2O_3)_{0.05}$	$(ZrO_2)_{0.93}$ $\cdot (Y_2O_3)_{0.07}$	$(ZrO_2)_{0.92}$ $\cdot (Y_2O_3)_{0.08}$	$(ZrO_2)_{0.90}$ $\cdot (Y_2O_3)_{0.10}$
Center	2910.87	2823.43	585.669	1269.14	1744.46	1008.72
Corner 1	2351.54	2081.02	1006.61	1569.93	1425.88	914.833
Corner 2	1683.01	1507.48	1568.13	2398.81	1485.69	1139.9
Corner 3	1392.55	1256.27	1582.71	1724.51	1115.78	1094.77
Corner 4	1151.17	1055.92	2075.26	1759.48	1264.83	660.176

Table 13: Average Sheet Resistance of 100 mJ onto Polished Silicon

Position	$(ZrO_2)_{0.99}$ $\cdot (Y_2O_3)_{0.01}$	$(ZrO_2)_{0.97}$ $\cdot (Y_2O_3)_{0.03}$	$(ZrO_2)_{0.95}$ $\cdot (Y_2O_3)_{0.05}$	$(ZrO_2)_{0.93}$ $\cdot (Y_2O_3)_{0.07}$	$(ZrO_2)_{0.92}$ $\cdot (Y_2O_3)_{0.08}$	$(ZrO_2)_{0.90}$ $\cdot (Y_2O_3)_{0.10}$
Center	4777.91	1671.48	2570.3	1266.34	1591.03	2456.14
Corner 1	2405.75	2609.53	2939.51	3012.8	2932.59	2594.48
Corner 2	3155.3	3735.56	2723.36	1963.25	982.892	3403.01
Corner 3	3312.78	2886.38	1455.95	1063.41	495.983	3980.18
Corner 4	4356.12	1316.94	3922.64	956.013	2181.91	1667.43

Table 14: Average Sheet Resistance of 120 mJ onto Polished Silicon

Similarly, to the four-point probe results, the resistivity results show an overall uniformity of the results for the layers produced with 100 mJ. Likewise, the values associated with the 120 mJ does show a wider range of values with more irregular data points compared to the 100 mJ data points. As later figures will show all the key data points will show an exponential decay with little change between the 100 mJ and 120 mJ for the Polished Zr and the Al_2O_3.

Position	$(ZrO_2)_{0.99}$ $\cdot (Y_2O_3)_{0.01}$	$(ZrO_2)_{0.97}$ $\cdot (Y_2O_3)_{0.03}$	$(ZrO_2)_{0.95}$ $\cdot (Y_2O_3)_{0.05}$	$(ZrO_2)_{0.93}$ $\cdot (Y_2O_3)_{0.07}$	$(ZrO_2)_{0.92}$ $\cdot (Y_2O_3)_{0.08}$	$(ZrO_2)_{0.90}$ $\cdot (Y_2O_3)_{0.10}$
Center	3.8969 E-4	2.0793 E-4	1.3136 E-4	3.6423 E-4	8.320 E-5	1.5909 E-4
Corner 1	4.6015 E-4	1.3685 E-4	5.9058 E-4	1.6014 E-4	6.751 E-5	2.3638 E-4
Corner 2	1.7212 E-4	3.4880 E-4	2.6197 E-4	1.3254 E-4	2.2246 E-4	1.5414 E-4
Corner 3	3.1237 E-4	1.9033 E-4	4.7174 E-4	1.3197 E-4	1.0591 E-4	1.0771 E-4
Corner 4	2.2150 E-4	1.7577 E-4	2.142 E-5	6.512 E-4	4.748 E-5	2.5013 E-4

Table 15: Resistivity value for 100 mJ on Polished Zirconium

Position	$(ZrO_2)_{0.99}$ $\cdot (Y_2O_3)_{0.01}$	$(ZrO_2)_{0.97}$ $\cdot (Y_2O_3)_{0.03}$	$(ZrO_2)_{0.95}$ $\cdot (Y_2O_3)_{0.05}$	$(ZrO_2)_{0.93}$ $\cdot (Y_2O_3)_{0.07}$	$(ZrO_2)_{0.92}$ $\cdot (Y_2O_3)_{0.08}$	$(ZrO_2)_{0.90}$ $\cdot (Y_2O_3)_{0.10}$
Center	3.3468 E-4	4.3669 E-4	2.1590 E-4	1.6804 E-4	1.3397 E-4	2.4326 E-4
Corner 1	2.9872 E-4	2.1708 E-4	8.838 E-5	7.739 E-5	1.8142 E-4	2.1018 E-4
Corner 2	4.0170 E-4	3.6472 E-4	2.6964 E-4	2.6656 E-4	1.0161 E-4	2.9156 E-4
Corner 3	3.5094 E-4	2.2717 E-4	2.7319 E-4	2.4744 E-4	1.0067 E-4	1.5204 E-4
Corner 4	1.4688 E-4	2.8024 E-4	9.094 E-5	2.1894 E-4	1.0146 E-4	1.3770 E-4

Table 16: Resistivity value for 120 mJ on Polished Zirconium

Position	$(ZrO_2)_{0.99}$ $\cdot (Y_2O_3)_{0.01}$	$(ZrO_2)_{0.97}$ $\cdot (Y_2O_3)_{0.03}$	$(ZrO_2)_{0.95}$ $\cdot (Y_2O_3)_{0.05}$	$(ZrO_2)_{0.93}$ $\cdot (Y_2O_3)_{0.07}$	$(ZrO_2)_{0.92}$ $\cdot (Y_2O_3)_{0.08}$	$(ZrO_2)_{0.90}$ $\cdot (Y_2O_3)_{0.10}$
Center	6.40773 E-4	6.1464 E-4	5.1849 E-4	5.2942 E-4	4.1745 E-4	4.7536 E-4
Corner 1	6.10089 E-4	6.0394 E-4	5.409 E-4	5.0513 E-4	4.5654 E-4	4.2766 E-4
Corner 2	6.02829 E-4	4.7983 E-4	5.6869 E-4	4.5793 E-4	4.5747 E-4	5.7251 E-4
Corner 3	6.29031 E-4	8.1626 E-4	5.2661 E-4	4.9986 E-4	4.4597 E-4	4.8959 E-4
Corner 4	6.14536 E-4	6.0257 E-4	5.2836 E-4	5.0374 E-4	3.8699 E-4	5.3428 E-4

Table 17: Resistivity value for 100 mJ on Polished Al_2O_3

Position	$(ZrO_2)_{0.99} \cdot (Y_2O_3)_{0.01}$	$(ZrO_2)_{0.97} \cdot (Y_2O_3)_{0.03}$	$(ZrO_2)_{0.95} \cdot (Y_2O_3)_{0.05}$	$(ZrO_2)_{0.93} \cdot (Y_2O_3)_{0.07}$	$(ZrO_2)_{0.92} \cdot (Y_2O_3)_{0.08}$	$(ZrO_2)_{0.90} \cdot (Y_2O_3)_{0.10}$
Center	6.97814 E-4	4.7959 E-4	5.0182 E-4	4.8058 E-4	4.8366 E-4	4.8375 E-4
Corner 1	6.01507 E-4	5.7012 E-4	5.3815 E-4	5.0166 E-4	5.7402 E-4	4.2923 E-4
Corner 2	6.16349 E-4	6.0562 E-4	8.4987 E-4	4.7852 E-4	5.2127 E-4	5.0063 E-4
Corner 3	6.19082 E-4	6.4514 E-4	5.0276 E-4	5.0489 E-4	5.1616 E-4	4.8956 E-4
Corner 4	6.2692 E-4	5.3732 E-4	6.11 E-4	4.6989 E-4	5.2691 E-4	4.6884 E-4

Table 18: Resistivity value for 120 mJ on Polished Al_2O_3

Position	$(ZrO_2)_{0.99} \cdot (Y_2O_3)_{0.01}$	$(ZrO_2)_{0.97} \cdot (Y_2O_3)_{0.03}$	$(ZrO_2)_{0.95} \cdot (Y_2O_3)_{0.05}$	$(ZrO_2)_{0.93} \cdot (Y_2O_3)_{0.07}$	$(ZrO_2)_{0.92} \cdot (Y_2O_3)_{0.08}$	$(ZrO_2)_{0.90} \cdot (Y_2O_3)_{0.10}$
Center	2.397393 E-3	2.22542 E-3	4.5987 E-4	9.9538 E-4	1.36347 E-3	7.7843 E-4
Corner 1	1.936728 E-3	1.63339 E-3	7.9582 E-4	1.22596 E-3	1.1196 E-3	7.0589 E-4
Corner 2	1.38192 E-3	1.18442 E-3	1.22392 E-3	1.88162 E-3	1.16003 E-3	8.7875 E-4
Corner 3	1.128382 E-3	9.8567 E-4	1.24465 E-3	1.35098 E-3	8.7109 E-4	8.4472 E-4
Corner 4	9.61453 E-4	8.2562 E-4	1.63012 E-3	1.38559 E-3	9.8391 E-4	5.0952 E-4

Table 19: Resistivity value for 100 mJ on Polished Silicon

Position	$(ZrO_2)_{0.99}$ $\cdot (Y_2O_3)_{0.01}$	$(ZrO_2)_{0.97}$ $\cdot (Y_2O_3)_{0.03}$	$(ZrO_2)_{0.95}$ $\cdot (Y_2O_3)_{0.05}$	$(ZrO_2)_{0.93}$ $\cdot (Y_2O_3)_{0.07}$	$(ZrO_2)_{0.92}$ $\cdot (Y_2O_3)_{0.08}$	$(ZrO_2)_{0.90}$ $\cdot (Y_2O_3)_{0.10}$
Center	3.752089 E-3	1.31145 E-3	1.99712 E-3	9.9775 E-4	1.24657 E-3	1.9261 E-3
Corner 1	1.887314 E-3	2.04665 E-3	2.29223 E-3	2.36565 E-3	2.29856 E-3	2.03044 E-3
Corner 2	2.471858 E-3	2.9283 E-3	2.11442 E-3	1.54527 E-3	7.7029 E-4	2.6683 E-3
Corner 3	2.605169 E-3	2.26119 E-3	1.13099 E-3	8.3733 E-4	3.8791 E-4	3.12126 E-3
Corner 4	3.420425 E-3	1.03327 E-3	3.04005 E-3	7.5382 E-4	1.70844 E-3	1.3071 E-3

Table 20: Resistivity value for 120 mJ on Polished Silicon

Scanning Electron Microscope

  The Scanning Electron Microscope images are twofold. Firstly, the characteristic of the surface of deposited layer. The images below shows that the deposited layer is overall uniform for all the deposited layers. Secondly, using the scale for each of the images a rough thickness of the deposited layer can be found. In the following images the deposited layer is highlighted in red to make it easier to see in comparison with the substrates.
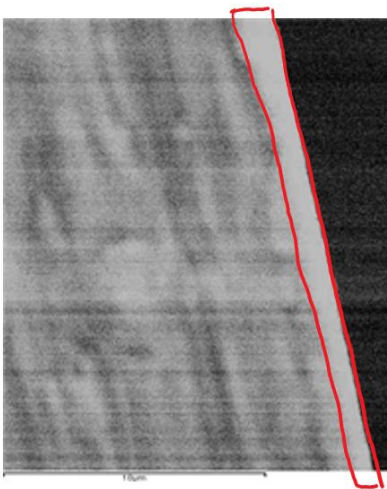
Figure 11: SEM imagery of $(ZrO_2)_{0.99} \cdot (Y_2O_3)_{0.01}$ on Polished Zr at 100 mJ

Figure 12: SEM imagery of $(ZrO_2)_{0.93} \cdot (Y_2O_3)_{0.07}$ on Polished Zr at 100 mJ
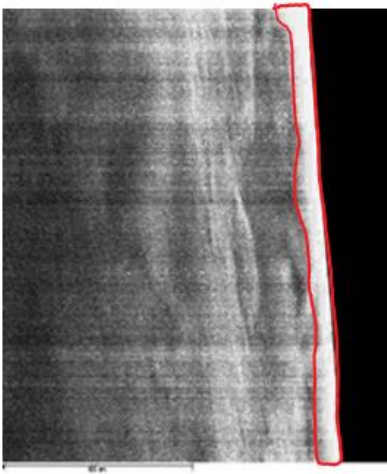
Figure 13: SEM imagery of $(ZrO_2)_{0.99} \cdot (Y_2O_3)_{0.01}$ on Polished Al_2O_3 at 100 mJ
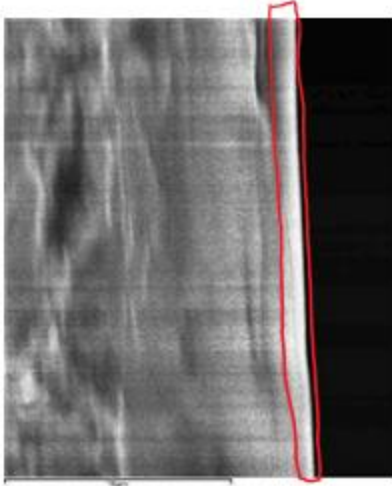
Figure 14: SEM imagery of $(ZrO_2)_{0.92} \cdot (Y_2O_3)_{0.08}$ on Polished Al_2O_3 at 100 mJ
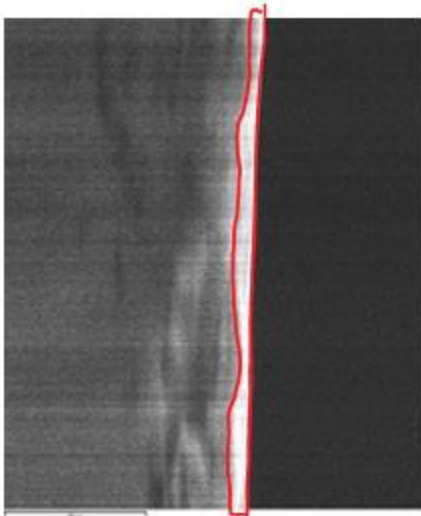
Figure 15: SEM imagery of $(ZrO_2)_{0.97} \cdot (Y_2O_3)_{0.03}$ on Polished Si at 100 mJ
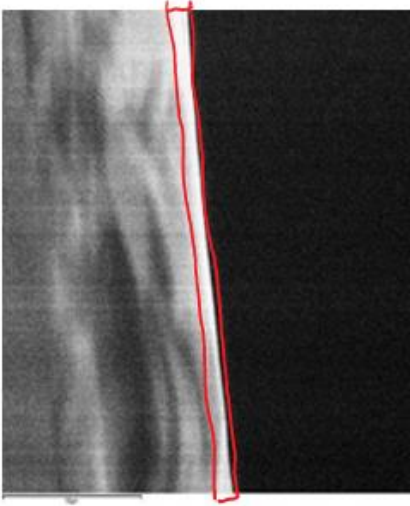
Figure 16: SEM imagery of $(ZrO_2)_{0.92} \cdot (Y_2O_3)_{0.08}$ on Polished Si at 100 mJ

Discussion

From the given data, the comparison between the various layers can be shown. The data shown for the various layers of $(ZrO_2)_{1-x} \cdot (Y_2O_3)_x$ on Polished Zirconium with 100 mJ of laser energy, as the concentration increases the resistivity values follow an exponential decay path. As the graph shows it plateaus at the $(ZrO_2)_{0.92} \cdot (Y_2O_3)_{0.08}$ concentration. Like the various layers of $(ZrO_2)_{1-x} \cdot (Y_2O_3)_x$ on Polished Zirconium with 100 mJ of laser energy, the various layers of $(ZrO_2)_{1-x} \cdot (Y_2O_3)_x$ on Polished Zirconium with 120 mJ of laser energy the resistivity values follows an exponential decay path and the graph plateaus at the $(ZrO_2)_{0.92} \cdot (Y_2O_3)_{0.08}$ concentration. Overlaying the two different graphs, the change in the laser energy does not a dramatic change in resistivity values. Also, the data shows that the Pulsed Laser Deposition method is a successful method of creating a thin film of $(ZrO_2)_{1-x} \cdot (Y_2O_3)_x$ onto Polished Zirconium with 100 mJ and 120 mJ of laser energy with little difference from the ideal thickness of 8000 Angstroms.

	Thickness	*Average Sheet Resistance*	*Resistivity*
$(ZrO_2)_{0.99} \cdot (Y_2O_3)_{0.01}$	7840	586.9213	4.6015 E-4
$(ZrO_2)_{0.97} \cdot (Y_2O_3)_{0.03}$	8481	411.2687	3.4880 E-4
$(ZrO_2)_{0.95} \cdot (Y_2O_3)_{0.05}$	7034	372.4276	2.6197 E-4
$(ZrO_2)_{0.93} \cdot (Y_2O_3)_{0.07}$	7774	205.9976	1.6014 E-4
$(ZrO_2)_{0.92} \cdot (Y_2O_3)_{0.08}$	7998	132.4166	1.0591 E-4
$(ZrO_2)_{0.90} \cdot (Y_2O_3)_{0.10}$	8961	120.2001	1.0771 E-4

Table 21: Key points for 100 mJ onto Polished Zirconium

	Thickness	Average Sheet Resistance	Resistivity
$(ZrO_2)_{0.99} \cdot (Y_2O_3)_{0.01}$	7886	509.3813	4.0170 E-4
$(ZrO_2)_{0.97} \cdot (Y_2O_3)_{0.03}$	7953	465.5544	3.7026 E-4
$(ZrO_2)_{0.95} \cdot (Y_2O_3)_{0.05}$	7961	271.1988	2.1590 E-4
$(ZrO_2)_{0.93} \cdot (Y_2O_3)_{0.07}$	7905	212.5696	1.6804 E-4
$(ZrO_2)_{0.92} \cdot (Y_2O_3)_{0.08}$	7903	169.5118	1.3397 E-4
$(ZrO_2)_{0.90} \cdot (Y_2O_3)_{0.10}$	7889	174.5478	1.3770 E-4

Table 22: Key points for 120 mJ onto Polished Zirconium
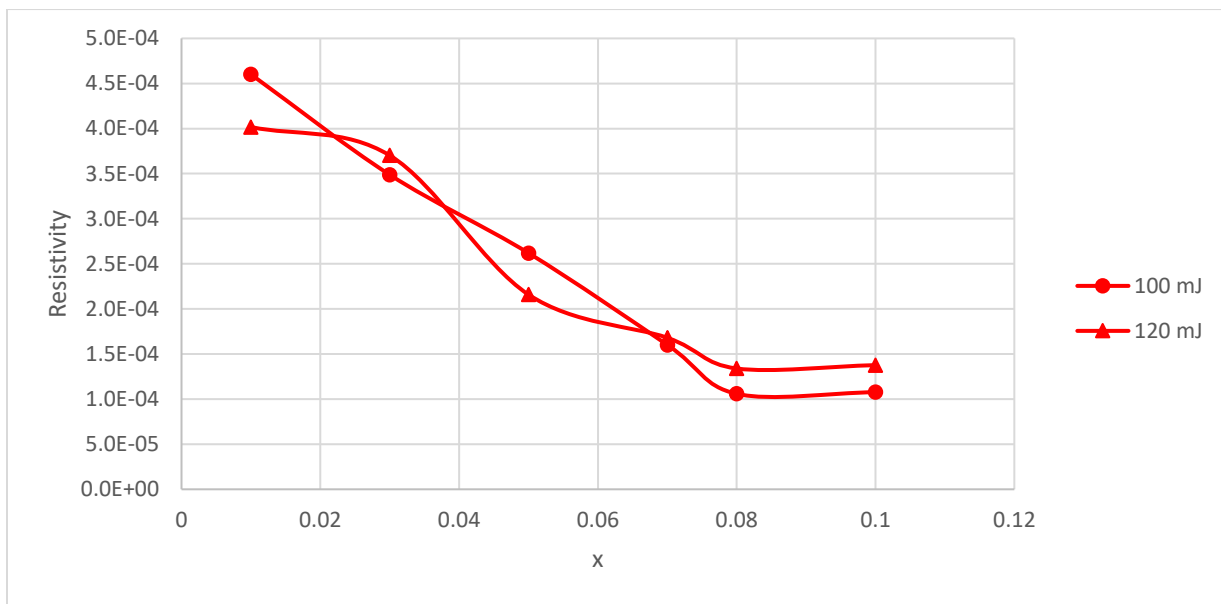
Figure 17: Graph for key points for 100 mJ and 120 mJ onto Polished Zirconium

The data shown for the various layers of $(ZrO_2)_{1-x} \cdot (Y_2O_3)_x$ on Polished Al_2O_3 with 100 mJ of laser energy and 120 mJ also follow an exponential decay path, just like the layers of $(ZrO_2)_{1-x} \cdot (Y_2O_3)_x$ on Polished Zirconium with 100 mJ of laser energy and 120 mJ. Similarly to the $(ZrO_2)_{1-x} \cdot (Y_2O_3)_x$ on Polished Zirconium with 100 mJ of laser energy and 120 mJ, the layers of $(ZrO_2)_{1-x} \cdot (Y_2O_3)_x$ on Polished Al_2O_3 with 100 mJ of laser energy and 120 mJ plateau at the

concentration of $(ZrO_2)_{0.92} \cdot (Y_2O_3)_{0.08}$. Overlaying the two different graphs, the change in the laser energy results in almost no change in the resistivity values. Also, the data shows that the Pulsed Laser Deposition method is a successful method of creating a thin film of $(ZrO_2)_{1-x} \cdot (Y_2O_3)_x$ onto Polished Al_2O_3 with 100 mJ and 120 mJ of laser energy with little difference from the ideal thickness of 8000 Angstroms, but it does appear to consistently be about 500 Angstroms thicker than what was expected.

	Thickness	Average Sheet Resistance	Resistivity
$(ZrO_2)_{0.99} \cdot (Y_2O_3)_{0.01}$	8560	740.5661	6.3392 E-4
$(ZrO_2)_{0.97} \cdot (Y_2O_3)_{0.03}$	8388	720.0041	6.0394 E-4
$(ZrO_2)_{0.95} \cdot (Y_2O_3)_{0.05}$	8556	632.1837	5.4090 E-4
$(ZrO_2)_{0.93} \cdot (Y_2O_3)_{0.07}$	8535	588.3428	5.0215 E-4
$(ZrO_2)_{0.92} \cdot (Y_2O_3)_{0.08}$	8094	550.9903	4.4597 E-4
$(ZrO_2)_{0.90} \cdot (Y_2O_3)_{0.10}$	8550	500.1888	4.2766 E-4

Table 23: Key points for 100 mJ onto Polished Al_2O_3

	Thickness	Average Sheet Resistance	Resistivity
$(ZrO_2)_{0.99} \cdot (Y_2O_3)_{0.01}$	8554	732.897	6.2692 E-4
$(ZrO_2)_{0.97} \cdot (Y_2O_3)_{0.03}$	8588	705.1881	6.0562 E-4
$(ZrO_2)_{0.95} \cdot (Y_2O_3)_{0.05}$	8572	627.7955	5.3815 E-4
$(ZrO_2)_{0.93} \cdot (Y_2O_3)_{0.07}$	8553	586.5261	5.0166 E-4
$(ZrO_2)_{0.92} \cdot (Y_2O_3)_{0.08}$	8549	565.7498	4.8366 E-4
$(ZrO_2)_{0.90} \cdot (Y_2O_3)_{0.10}$	8546	502.2615	4.2923 E-4

Table 24: Key points for 120 mJ onto Polished Al_2O_3
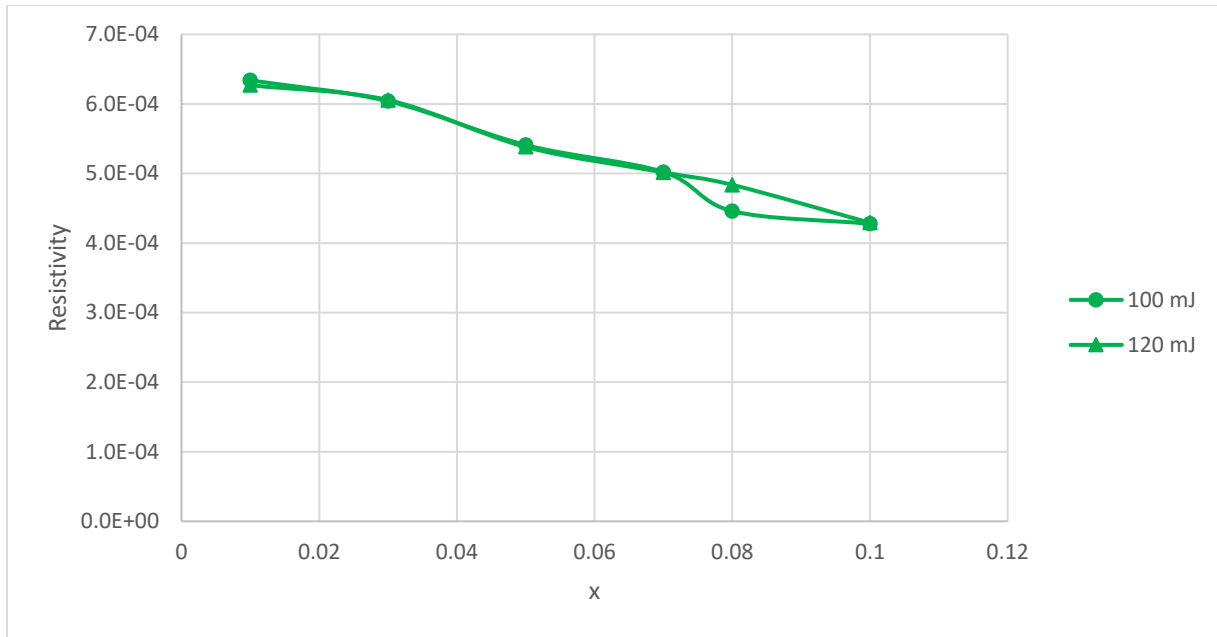
Figure 18: Graph for key points for 100 mJ and 120 mJ onto Polished Al_2O_3

The data shown for the various layers of $(ZrO_2)_{1-x} \cdot (Y_2O_3)_x$ on Polished Silicon with 100 mJ of laser energy and 120 mJ also follow an exponential decay path, just like the layers of $(ZrO_2)_{1-x} \cdot (Y_2O_3)_x$ on Polished Zirconium and Polished Al_2O_3 with 100 mJ of laser energy and 120 mJ. Similarly to the $(ZrO_2)_{1-x} \cdot (Y_2O_3)_x$ on Polished Zirconium and Polished Al_2O_3 with 100 mJ of laser energy and 120 mJ, the layers of $(ZrO_2)_{1-x} \cdot (Y_2O_3)_x$ on Polished Silicon with 100 mJ of laser energy and 120 mJ plateau at the concentration of $(ZrO_2)_{0.92} \cdot (Y_2O_3)_{0.08}$. Overlaying the two different graphs, the data shows that changing the laser energy value results in a large change in resistivity values. Also, the data shows that the Pulsed Laser Deposition method is a successful method of creating a thin film of $(ZrO_2)_{1-x} \cdot (Y_2O_3)_x$ onto Polished Silicon with 100 mJ and 120 mJ of laser energy with little difference from the ideal thickness of 8000 Angstroms.

	Thickness	Average Sheet Resistance	Resistivity
$(ZrO_2)_{0.99} \cdot (Y_2O_3)_{0.01}$	8236	2351.539	1.93673 E-3
$(ZrO_2)_{0.97} \cdot (Y_2O_3)_{0.03}$	7849	2081.019	1.63339 E-3
$(ZrO_2)_{0.95} \cdot (Y_2O_3)_{0.05}$	7864	1582.714	1.24465 E-3
$(ZrO_2)_{0.93} \cdot (Y_2O_3)_{0.07}$	7843	1269.138	9.9538 E-4
$(ZrO_2)_{0.92} \cdot (Y_2O_3)_{0.08}$	7807	1115.775	8.7109 E-4
$(ZrO_2)_{0.90} \cdot (Y_2O_3)_{0.10}$	7717	1008.718	7.7843 E-4

Table 25: Key points for 100 mJ onto Polished Silicon

	Thickness	Average Sheet Resistance	Resistivity
$(ZrO_2)_{0.99} \cdot (Y_2O_3)_{0.01}$	7834	3155.295	2.47186 E-3
$(ZrO_2)_{0.97} \cdot (Y_2O_3)_{0.03}$	7834	2886.383	2.26119 E-3
$(ZrO_2)_{0.95} \cdot (Y_2O_3)_{0.05}$	7770	2570.298	1.99712 E-3
$(ZrO_2)_{0.93} \cdot (Y_2O_3)_{0.07}$	7871	1963.245	1.54527 E-3
$(ZrO_2)_{0.92} \cdot (Y_2O_3)_{0.08}$	7835	1591.032	1.24657 E-3
$(ZrO_2)_{0.90} \cdot (Y_2O_3)_{0.10}$	7839	1667.429	1.30710 E-3

Table 26: Key points for 120 mJ onto Polished Silicon
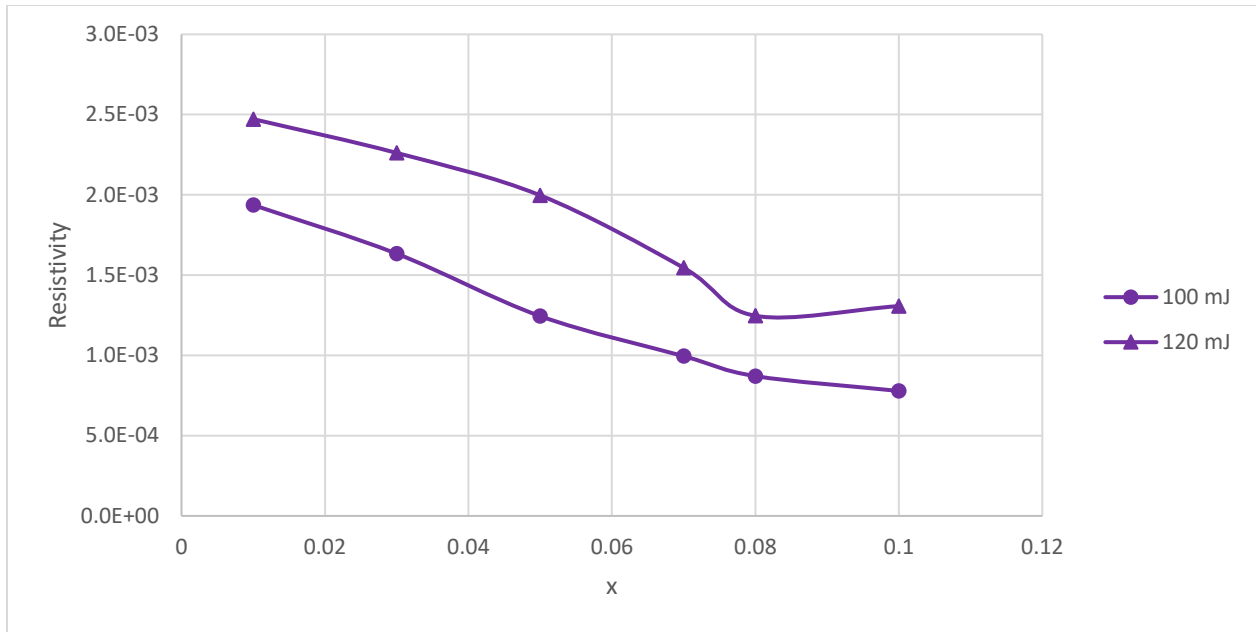
Figure 19: Graph for key points for 100 mJ and 120 mJ onto Polished Silicon

When comparing Polished Zirconium, Polished Al_2O_3, and Polished Silicon at 100 mJ and 120 mJ laser energy, the data shows the variation of the different substrates well. It is shown that the substrates that have the lowest resistivity to highest resistivity are in the given order of Polished Zirconium, Polished Al_2O_3, and Polished Silicon. With the lowest resistivity value being the $(ZrO_2)_{0.92} \cdot (Y_2O_3)_{0.08}$ on Polished Zirconium with 100 mJ as a laser energy and the highest being $(ZrO_2)_{0.99} \cdot (Y_2O_3)_{0.01}$ on Polished Silicon with 120 mJ as a laser energy.
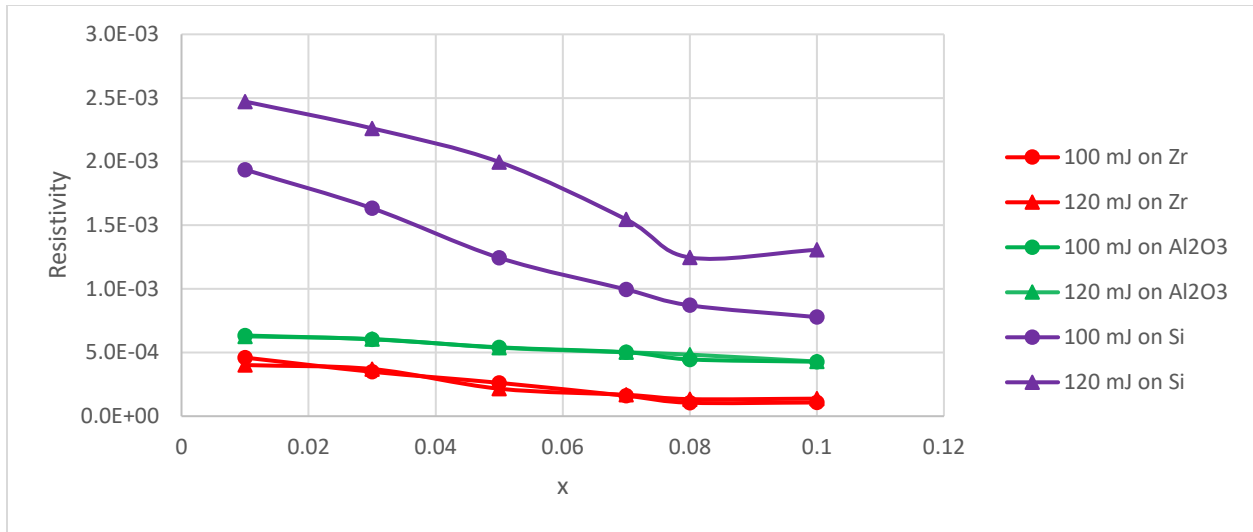
Figure 20: Comparison of Polished Zirconium, Polished Al2O3, and Polished Silicon with 100 mJ and 120 mJ

As all the data shown, the methodology on producing the electrolyte layer on various substrates has proven to be a viable and repeatable process with little differences from the ideal thickness.

Conclusion

As previously shown, the Pulsed Laser Deposition method can produce the different concentrations of a YSZ electrolyte layer on multiple different substrates. According to the data for the Polished Zr Al_2O_3, and Si, the 120 mJ samples have a closer thickness to the optimal thickness. In addition, the 120 mJ has a better repetition of the same thickness than the 100 mJ. The resistivity values for each substrate and energy levels followed an exponential decay pathing when increasing the concentration. Making the $(ZrO_2)_{0.92} \cdot (Y_2O_3)_{0.08}$ Polished Zr with 100 mJ the lowest value.

Work Cited

1) Wachsman, Eric D., and Kang Taek Lee. "Lowering the Temperature of Solid Oxide Fuel Cells." *Science*, American Association for the Advancement of Science, 2011

2) Noriko Hikosaka Behling, Chapter 2 - Fuel Cells and the Challenges Ahead, Fuel Cells, Elsevier, 2013

3) Minh, N.Q., Ceramic Fuel Cells. Journal of the American Ceramic Society, 1993

4) M. Muthukumar, N. Rengarajan, B. Velliyangiri, M.A. Omprakas, C.B. Rohit, U. Kartheek Raja, The development of fuel cell electric vehicles – A review,Materials Today: Proceedings, 2020

5) P.J de Wild, M.J.F.M Verhaak, Catalytic production of hydrogen from methanol, Catalysis Today, Volume 60, Issues 1–2, 2000

6) Paul Breeze, Chapter 1 - An Introduction to Fuel Cells, Fuel Cells, Academic Press, 2017

7) Grove, W. R. "On the Gas Voltaic Battery. Experiments Made with a View of Ascertaining the Rationale of Its Action and Its Application to Eudiometry." *Philosophical Transactions of the Royal Society of London*, vol. 133, 1843

8) Sammes N.M., Bove R., Pusz J. Solid Oxide Fuel Cells. Fuel Cell Technology. Engineering Materials and Processes. Springer, London, 2006

9) Curtin, Sandra, and Jennifer Gangi. *Fuel Cell Technologies Market Report 2016*. U.S. Department of Energy, 2016.

10) Žiliukas, Antanas. *An Overview of Fuel Cells Application in Transportation*. Transport, Vol XIX, Oct. 2004, Page 219-223

11) Jackson, Lisa. *Environmental Responsibility Report*. Apple, 2016.

12) *Bloom Energy Completes Fuel Cell Project at Morgan Stanley Global Headquarters in New York City*, 29 June 2018,

13) Roth, Joseph. "IKEA Plugs-in More Onsite Power in Costa Mesa and Covina, CA as Fuel Cell Systems Expand Retailer's Renewable Energy Portfolio." *IKEA Plugs-in More Onsite Power in Costa Mesa and Covina, CA as Fuel Cell Systems Expand Retailer's Renewable Energy Portfolio | Business Wire*, Businesswire, 17 Nov. 2016

14) Otero, Jordan. *West Hartford Manufacturer Flicks Switch On New Fuel Cell*. Hartford Courant, 12 Dec. 2018,

15) Behling, Noriko Hikosaka. *Fuel Cells: Current Technology Challenges and Future Research Needs*. Elsevier, 2013.

16) Irshad, Muneeb. *A Brief Description of High Temperature Solid Oxide Fuel Cell's Operation, Materials, Design, Fabrication Technologies and Performance*. Applied Sciences, 2016.

17) Chia-Lien Lu, Cheng-Ping Chang, Yi-Hsuan Guo, Tsung-Kuang Yeh, Yu-Chuan Su, Pen-Cheng Wang, Kan-Lin Hsueh, Fan-Gang Tseng, High-performance and low-leakage phosphoric acid fuel cell with synergic composite membrane stacking of micro glass microfiber and nano PTFE, Renewable Energy, Volume 134, 2019, Pages 982-988,

18) "Comparison of Fuel Cell Technologies." *Energy.gov*,

19) Scott A. Mauger, Jason R. Pfeilsticker, Min Wang, Samantha Medina, A.C. Yang-Neyerlin, K.C. Neyerlin, Caleb Stetson, Svitlana Pylypenko, Michael Ulsh, Fabrication of high-performance gas-diffusion-electrode based membrane-electrode assemblies, Journal of Power Sources, Volume 450, 2020,

20) Xinnru Guo, Houcheng Zhang, Performance analyses of a combined system consisting of high-temperature polymer electrolyte membrane fuel cells and thermally regenerative electrochemical cycles, Energy, Volume 193, 2020,

21) Yang Zhao, Xue Li, WeiWei Li, Zhongyang Wang, Shubo Wang, Xiaofeng Xie, Vijay Ramani, A high-performance membrane electrode assembly for polymer electrolyte membrane fuel cell with poly(arylene ether sulfone) nanofibers as effective membrane reinforcements, Journal of Power Sources, Volume 444, 2019,

22) G.F. McLean, T. Niet, S. Prince-Richard, N. Djilali, An assessment of alkaline fuel cell technology, International Journal of Hydrogen Energy, Volume 27, Issue 5, 2002, Pages 507-526,

23) Dibyendu Roy, Samiran Samanta, Sudip Ghosh, Performance assessment of a biomass-fuelled distributed hybrid energy system integrating molten carbonate fuel cell, externally fired gas turbine and supercritical carbon dioxide cycle, Energy Conversion and Management, Volume 211, 2020,

24) Ruth, Mark. *Independent Review Panel for 1–10 KW Stationary Combined Heat and Power Systems Status and Technical Potential*. National Renewable Energy Laboratory, 2010.

25) Maria Cristina Tanzi, Silvia Farè, Gabriele Candiani, Chapter 4 - Biomaterials and Applications, Editor(s): Maria Cristina Tanzi, Silvia Farè, Gabriele Candiani, Foundations of Biomaterials Engineering, Academic Press, 2019, Pages 199-287,

26) William J. Tropf, Michael E. Thomas, - Yttrium Oxide (Y2O3), Editor(s): Edward D. Palik, Handbook of Optical Constants of Solids, Academic Press, 1997, Pages 1079-1096,

27) Mark C. Williams, Chapter 2 - Fuel Cells, Editor(s): Dushyant Shekhawat, James J. Spivey, David A. Berry, Fuel Cells: Technologies for Fuel Processing, Elsevier, 2011, Pages 11-27,

28) Ibrahim Dincer, Marc A. Rosen, Chapter 1 - Thermodynamic Fundamentals, Editor(s): Ibrahim Dincer, Marc A. Rosen, Exergy (Second Edition), Elsevier, 2013, Pages 1-20,

29) J. Pou, F. Lusquiños, R. Comesaña, M. Boutinguiza, Chapter 14 - Production of Biomaterial Coatings by Laser-Assisted Processes, Editor(s): Jonathan Lawrence, In Woodhead Publishing Series in Welding and Other Joining Technologies, Advances in Laser Materials Processing (Second Edition), Woodhead Publishing, 2018, Pages 381-412,

30) Quanhe Bao, Chuanzhong Chen, Diangang Wang, Qianmao Ji, Tingquan Lei, Pulsed laser deposition and its current research status in preparing hydroxyapatite thin films, Applied Surface Science, Volume 252, Issue 5, 2005, Pages 1538-1544,

31) Veli-Matti Airaksinen, Chapter 15 - Silicon Wafer and Thin Film Measurements, Editor(s): Markku Tilli, Teruaki Motooka, Veli-Matti Airaksinen, Sami Franssila, Mervi Paulasto-Kröckel, Veikko Lindroos, In Micro and Nano Technologies, Handbook of Silicon Based MEMS Materials and Technologies (Second Edition), William Andrew Publishing, 2015, Pages 381-390,

32) "What Is Ellipsometry?" *J.A. Woollam*, 12 Nov. 2019,

33) Biswas, Tamal. "Four-Point Probe Manual." *Academia.edu*

34) Waremra, Richard S., and Philipus Betaubun. *Analysis of Electrical Properties Using the Four Point Probe Method* . ICENIS, 2018.

35) Scanning Electron Microscopy (SEM)." *Techniques*, 26 May 2017,